

Effective finite-difference modelling methods with 2-D acoustic wave equation using a combination of cross and rhombus stencils

Enjiang Wang,^{1,2} Yang Liu^{1,2} and Mrinal K. Sen³

¹State Key Laboratory of Petroleum Resources and Prospecting, China University of Petroleum, Beijing, China. E-mail: wliuyang@vip.sina.com

²CNPC Key Laboratory of Geophysical Prospecting, China University of Petroleum, Beijing, China

³The Institute for Geophysics, John A. and Katherine G. Jackson School of Geosciences, The University of Texas at Austin, 10100 Burnet Road, R2200 Austin, TX 78758, USA

Accepted 2016 June 29. Received 2016 June 28; in original form 2016 March 4

SUMMARY

The 2-D acoustic wave equation is commonly solved numerically by finite-difference (FD) methods in which the accuracy of solution is significantly affected by the FD stencils. The commonly used cross stencil can reach either only second-order accuracy for space domain dispersion-relation-based FD method or $(2M)$ th-order accuracy along eight specific propagation directions for time–space domain dispersion-relation-based FD method, if the conventional $(2M)$ th-order spatial FD and second-order temporal FD are used to discretize the equation. One other newly developed rhombus stencil can reach arbitrary even-order accuracy. However, this stencil adds significantly to computational cost when the operator length is large. To achieve a balance between the solution accuracy and efficiency, we develop a new FD stencil to solve the 2-D acoustic wave equation. This stencil is a combination of the cross stencil and rhombus stencil. A cross stencil with an operator length parameter M is used to approximate the spatial partial derivatives while a rhombus stencil with an operator length parameter N together with the conventional second-order temporal FD is employed in approximating the temporal partial derivatives. Using this stencil, a new FD scheme is developed; we demonstrate that this scheme can reach $(2M)$ th-order accuracy in space and $(2N)$ th-order accuracy in time when spatial FD coefficients and temporal FD coefficients are derived from respective dispersion relation using Taylor-series expansion (TE) method. To further increase the accuracy, we derive the FD coefficients by employing the time–space domain dispersion relation of this FD scheme using TE. We also use least-squares (LS) optimization method to reduce dispersion at high wavenumbers. Dispersion analysis, stability analysis and modelling examples demonstrate that our new scheme has greater accuracy and better stability than conventional FD schemes, and thus can adopt large time steps. To reduce the extra computational cost resulting from adopting the new stencil, we apply the variable spatial operator length schemes. Adopting our new FD scheme, characterized by new stencil, LS-based optimization, variable operator lengths and larger time step, modelling efficiency is significantly improved.

Key words: Numerical solutions; Wave propagation.

1 INTRODUCTION

Applications of reverse-time migration (e.g. Baysal *et al.* 1983; McMechan 1983; Virieux *et al.* 2011) and full-waveform inversion (e.g. Tarantola 1984; Pratt *et al.* 1998; Virieux & Operto 2009; Bae *et al.* 2012) in exploration geophysics require accurate and stable simulation of seismic wavefields in the subsurface. Many simulation methods, such as finite-element (e.g. Marfurt 1984; Ichimura *et al.* 2007; Moczo *et al.* 2010, 2011), finite-difference (FD; e.g. Virieux 1984; Levander 1988; Lele 1992; Moczo *et al.* 2011; Zhang *et al.* 2014) and pseudospectral (e.g. Kosloff & Baysal 1982; Fornberg 1987; Furumura & Takenaka 1996), have been developed. The FD method is usually preferred due to its easy implementation and low requirement of computational resources. A comprehensive introduction about applications of FD methods in seismology is given in Moczo *et al.* (2014). Over the past several decades, many studies have focused on determining FD coefficients and designing FD stencils.

The FD methods can be divided into space-domain and time–space-domain ones depending on the methods used to determine the FD coefficients. The space-domain FD (Dablain 1986) determines the spatial FD coefficients using the space-domain dispersion relation,

which measures only the accuracy of FD approximation to the spatial partial derivative. Without consideration of wave propagating in the time domain, this scheme is prone to dispersion. In contrast, time–space-domain FD determines the spatial FD coefficients using the time–space-domain dispersion relation, which measures the accuracy of FD approximation to the exact wave equation. This scheme was reported to exhibit higher accuracy and better stability (e.g. Finkelstein & Kastner 2007, 2008; Liu & Sen 2009) than the space-domain FD. So far, there are mainly two kinds of time–space-domain FD. One was developed by Finkelstein & Kastner (2007, 2008), who compute the FD coefficients by satisfying the time–space-domain dispersion relation at some designated frequencies without any approximation. Another one was developed by Liu & Sen (2009), who determine the FD coefficients by minimizing the errors of time–space-domain dispersion relations over the continuous frequency band. The latter is more accurate because it can achieve high accuracy over wider frequency ranges rather than only at some designated frequencies.

FD coefficients can be determined by either Taylor-series expansion (TE; e.g. Dablain 1986; Finkelstein & Kastner 2007; Liu & Sen 2009; Chu & Stoffa 2012; Tan & Huang 2014b) or optimization methods (e.g. Tam & Webb 1993; Geller & Takeuchi 1998; Zhou & Zhang 2011; Zhang & Yao 2012a,b; Liu 2013, 2014). We name the schemes determining the coefficients using TE method as TE-based FD schemes, and those determining the coefficients using optimization methods as optimization-based FD schemes. In TE-based FD schemes, trigonometric functions in either the space-domain or the time–space-domain dispersion relation are expanded into polynomials using TE, and FD coefficients are obtained by solving a series of equations derived from comparing the polynomial coefficients on both sides of the dispersion relation. In optimization-based FD schemes, local or global optimization algorithms are used to compute the coefficients by minimizing errors of space-domain dispersion relation, time–space-domain dispersion relation, phase velocities, or group velocities within the given bandwidth. Regularizing techniques (Wang *et al.* 2014) were also introduced to provide more stable solutions of the FD coefficients. Of such two kinds of FD schemes, the TE-based schemes require the least computation cost and achieve high accuracy over the lower wavenumber range. However, beyond that, the accuracy decreases rapidly. By contrast, optimization-based schemes usually require much more computation cost since iterations are often involved but can obtain higher accuracy over wider wavenumber range. Liu (2013) developed an effective and efficient least-squares (LS) optimization-based FD scheme for second-order acoustic equation and proved that it can yield high accuracy and broaden the effective wavenumber range with moderate computational cost. Its main idea is to minimize dispersion under the specified accuracy and operator length in an LS sense. The objective functions are second-order multivariate functions with respect to FD coefficients and the globally optimal solution can be obtained by directly solving the linear equations without iterations. Liu (2014) further extended this method into the staggered grid FD schemes.

FD stencils define the number and distribution of the grid points involved in approximating the partial derivatives, thus they affect the accuracy of approximation significantly. So far, there are mainly two kinds of centred-grid FD stencils for solving the 2-D constant-density acoustic wave equation. One is the most widely used cross stencil (e.g. Dablain 1986; Liu & Sen 2009), in which spatial partial derivatives along horizontal and vertical axes are calculated by the grid points on the horizontal axis and vertical axis independently using high-order FD approximation. Adopting this stencil, the conventional space-domain centred-grid FD scheme can only achieve second-order accuracy when $(2M)$ th-order spatial FD and second-order temporal FD schemes are used to solve the second-order constant-density acoustic equation. When $2M$ approaches the total number of grid points along one axis, this scheme becomes the pseudospectral scheme (e.g. Kosloff & Baysal 1982; Fornberg 1987). Under the same discretization style as conventional space-domain centred-grid FD, the improved time–space-domain FD scheme (Liu & Sen 2009) can reach $(2M)$ th-order accuracy along eight specific propagation directions, thus it is more accurate. The other one is the rhombus stencil (Liu & Sen 2013), in which, the Laplace partial derivatives are approximated by a special diamond-shape FD stencil. Based on this stencil, the time–space domain dispersion-relation-based FD scheme yields $(2M)$ th-order accuracy along all propagation directions in both time and space when operator length parameter M is used, thus both the temporal and spatial dispersions are well suppressed. This scheme tends to be a perfect one for solving 2-D acoustic wave equation. However, it is computationally expensive because the number of the grid points involved is proportional to M^2 rather than M in the cross stencil. Motivated by the work of Liu & Sen (2013), Tan & Huang (2014a,b) proposed a staggered-grid FD scheme with $(2M)$ th-order accuracy in space and fourth- or sixth-order accuracy in time. Unlike the rhombus FD stencil, this scheme adopts the stencils that contain only a few more grid points off the axis than the cross stencil, that is, four for the fourth-order temporal accuracy and twelve for the sixth-order temporal accuracy. This scheme was demonstrated to be computationally more efficient than the standard staggered-grid FD scheme since larger time steps can be adopted. Both the TE (Tan & Huang 2014b) and Levenberg–Marquardt optimization (Tan & Huang 2014a) methods are used to determine the FD coefficients, based on the time–space-domain dispersion relation. It was proved that this scheme is similar to the Lax–Wendroff FD scheme (e.g. Lax & Wendroff 1960; Carcione *et al.* 2002; Chen 2007, 2009; Moczo *et al.* 2014). However, it is preferable over Lax–Wendroff FD scheme due to its easy implementation and less requirement of floating-point operations.

In recent years, many other effective FD schemes have been developed based on the exact time marching formula of the wave equation (e.g. Song & Fomel 2011; Song *et al.* 2013; Fang *et al.* 2014; Liu *et al.* 2014). All these methods were reported to exhibit significant improvements in temporal accuracy and stability. One common characteristic of these methods is the inevitability of dealing with the mixed space-wavenumber extrapolation operator. For solving the second-order acoustic wave equation, Song & Fomel (2011) first proposed to approximate the mixed space-wavenumber operator by cascading a Fourier transform operator and an FD operator, and developed the Fourier FD method. Song *et al.* (2013) further approximated the mixed space-wavenumber operator by using the lowrank decomposition, and developed the lowrank FD and lowrank Fourier FD methods. Those methods compute the FD coefficients at all locations simultaneously by complicated lowrank matrix decomposition. Also, those methods need to store FD coefficients at all the locations requiring large amounts

of memory, especially for large-scale model. Liu *et al.* (2014) proposed to approximate the mixed space–wavenumber operator using cosine basis functions, and proposed the explicit time evolution FD scheme. They adopted an FD stencil that includes four off-axial points. The FD coefficients are determined by minimizing evolution errors at some designated wavenumbers using LS method in the joint time–space domain. For solving the scalar wave equation, Fang *et al.* (2014) developed the lowrank FD method (Song *et al.* 2013) into the staggered grid. This kind of scheme demands a large amount of memory to store the FD coefficients.

In this paper, we develop a novel FD stencil for 2-D constant-density acoustic wave equation. In our proposed stencil, spatial derivatives are approximated by a cross stencil using an operator length parameter M and temporal derivatives are approximated by the conventional second-order FD plus a rhombus stencil using an operator length parameter N . This stencil contains $2N^2 - 2N$ more grid points off the axis than the cross stencil. If N equals 1, this stencil becomes the standard cross stencil and if N equals M , it is retrogressed into the rhombus stencil. Using this stencil, we develop a new FD scheme that can reach $(2M)$ th-order accuracy in space and $(2N)$ th-order accuracy in time respectively when spatial and temporal FD coefficients are determined by their respective dispersion relation using TE. To further increase the accuracy, we also use the time–space-domain dispersion relation of this new FD scheme to determine FD coefficients adopting TE method. The LS method is further used to improve the accuracy for high wavenumber components. Dispersion analysis, stability analysis and numerical modelling demonstrate that, our new schemes exhibit higher accuracy and better stability than both the conventional space-domain and time–space-domain cross-stencil based centred-grid FD schemes for solving the 2-D second-order acoustic wave equation. Moreover, our new schemes require less computational cost than the rhombus-stencil based FD scheme; thus they maintain a balance between accuracy and efficiency.

This paper is organized as follows. We first introduce our new FD stencil and FD scheme with $(2M)$ th-order accuracy in space and $(2N)$ th-order accuracy in time. Then we derive FD coefficients in this new stencil using TE method and LS method respectively based on the time–space-domain dispersion relation. This is followed by dispersion and stability analyses. Numerical modelling in homogeneous and heterogeneous models is conducted as well. In Section 6, we compare the accuracy of the conventional and new stencils for the same number of involved grid points. Finally, we draw conclusions based on these analyses.

2 FD MODELLING METHODS WITH A NEW STENCIL

In this section, we first introduce our new FD scheme in detail and show some kinds of retrogression of it. Then we derive the corresponding FD coefficients using the TE method and least-square optimization method respectively, based on the time–space-domain dispersion relation.

2.1 New FD schemes with $(2M)$ th-order spatial and $(2N)$ th-order temporal accuracies for 2-D acoustic wave equation

The 2-D acoustic wave equation in constant-density media can be described as

$$\frac{\partial^2 P}{\partial x^2} + \frac{\partial^2 P}{\partial z^2} = \frac{1}{v^2} \frac{\partial^2 P}{\partial t^2}, \quad (1)$$

where, $P(x, z, t)$ is the pressure and $v(x, z)$ is the velocity.

To approximate the spatial partial derivatives, we use the standard cross stencil, which is displayed in Fig. 1(a). The corresponding FD scheme is expressed as follows:

$$\frac{\partial^2 P}{\partial x^2} + \frac{\partial^2 P}{\partial z^2} \approx \frac{1}{h^2} \left[a'_0 P_{0,0}^0 + \sum_{m=1}^M a'_m (P_{-m,0}^0 + P_{m,0}^0 + P_{0,-m}^0 + P_{0,m}^0) \right], \quad (2)$$

where, $P_{m,n}^k = P(x + mh, z + nh, t + k\tau)$, h is the grid spacing, τ is the time step, M is the operator length parameter, a'_m are the FD coefficients and they can be obtained using the following equations:

$$a'_0 = -4 \sum_{m=1}^M a'_m, \quad (3a)$$

$$a'_m = \frac{(-1)^{m+1}}{m^2} \frac{\prod_{i=1, i \neq m}^M i^2}{\prod_{i=1}^{m-1} (m^2 - i^2) \prod_{i=m+1}^M (i^2 - m^2)}. \quad (3b)$$

Eqs (3a) and (3b) are derived from the spatial dispersion relation using TE and it has been proved that, when eqs (2) and (3) are used, the accuracy in space is $(2M)$ th-order.

Many methods, such as Adams–Bashforth/Moulton predictor–corrector scheme (Ghrist *et al.* 2000), Runge–Kutta method (e.g. Mead & Renaut 1999; Yang *et al.* 2007) and Lax–Wendroff FD scheme (e.g. Lax & Wendroff 1960; Chen 2007, 2009), have been proposed to increase the temporal accuracy. Here, we resort to one more convenient and easier way by introducing a special FD stencil. Liu & Sen (2013)

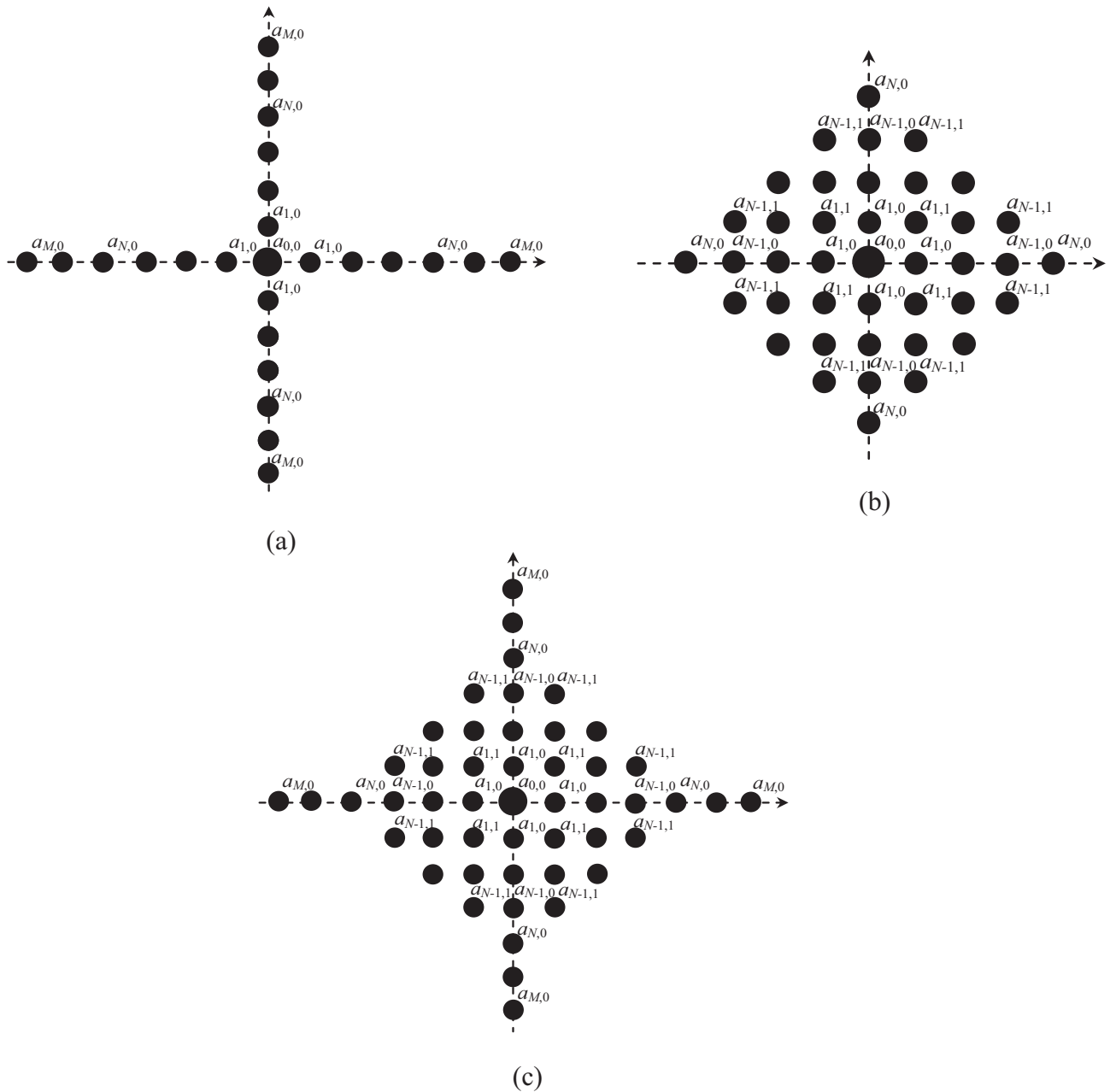


Figure 1. Illustrations of FD stencils for 2-D constant-density acoustic wave equation. (a) The conventional stencil (cross stencil). (b) The rhombus stencil. (c) The new stencil (cross stencil + rhombus stencil).

developed a rhombus stencil shown in Fig. 1(b) and proved that FD scheme adopting this stencil can reach the same high-order accuracy in both time and space along all directions. Therefore, we introduce this rhombus FD stencil into the conventional second-order temporal FD scheme to reach high-order accuracy in time. This new FD scheme used to approximate temporal derivative is expressed as follows:

$$\begin{aligned} \frac{\partial^2 P}{\partial t^2} \approx \frac{1}{\tau^2} [-2P_{0,0}^0 + (P_{0,0}^{-1} + P_{0,0}^1)] - \frac{v^2}{h^2} & \left[\sum_{m=1}^{N-1} \sum_{n=1}^{N-m} a''_{m,n} (P_{-m,-n}^0 + P_{m,n}^0 + P_{-m,n}^0 + P_{m,-n}^0) \right] \\ - \frac{v^2}{h^2} & \left[a''_{0,0} P_{0,0}^0 + \sum_{m=1}^N a''_{m,0} (P_{-m,0}^0 + P_{m,0}^0 + P_{0,-m}^0 + P_{0,m}^0) \right], \end{aligned} \quad (4)$$

where, $a''_{m,n}$ are the FD coefficients. Following a derivation similar to that described in Liu & Sen (2013) using TE, the FD coefficients can be determined by the following equations:

$$a''_{0,0} + 4 \sum_{m=1}^N a''_{m,0} + 4 \sum_{m=1}^{N-1} \sum_{n=1}^{N-m} a''_{m,n} = 0, \quad (5a)$$

$$\sum_{m=1}^N m^2 a''_{m,0} + 2 \sum_{m=1}^{N-1} \sum_{n=1}^{N-m} m^2 a''_{m,n} = 0, \quad (5b)$$

$$\sum_{m=1}^N m^{2j} a''_{m,0} + 2 \sum_{m=1}^{N-1} \sum_{n=1}^{N-m} m^{2j} a''_{m,n} = r^{2j-2} \quad (j = 2, 3, \dots, N), \quad (5c)$$

$$2 \sum_{m=1}^{N-1} \sum_{n=1}^{N-m} \frac{m^{2j-2\xi} n^{2\xi}}{(2j-2\xi)!(2\xi)!} a''_{m,n} = \frac{j! r^{2j-2}}{(2j)!\xi!(j-\xi)!} \quad (\xi = 1, 2, \dots, \text{int}(j/2), j = 2, \dots, N), \quad (5d)$$

where, int is a function to get the integer part of a real number.

It can be proved that the accuracy in time is $(2N)$ th-order when eqs (4) and (5) are used.

Substituting eqs (2) and (4) into eq. (1) and then rearranging eq. (1), we have,

$$\begin{aligned} \frac{1}{h^2} & \left[a_{0,0} P_{0,0}^0 + \sum_{m=1}^M a_{m,0} (P_{-m,0}^0 + P_{m,0}^0 + P_{0,-m}^0 + P_{0,m}^0) \right] + \frac{1}{h^2} \left[\sum_{m=1}^{N-1} \sum_{n=1}^{N-m} a_{m,n} (P_{-m,-n}^0 + P_{m,n}^0 + P_{-m,n}^0 + P_{m,-n}^0) \right] \\ & \approx \frac{1}{v^2 \tau^2} [-2P_{0,0}^0 + (P_{0,0}^{-1} + P_{0,0}^1)], \end{aligned} \quad (6)$$

where, $a_{m,n}$ are the same as $a''_{m,n}$, $a_{m,0}$ are linear combinations of a'_m and $a''_{m,0}$.

Eq. (6) is the FD scheme we adopt to solve the acoustic wave equation. The corresponding FD stencil is displayed in Fig. 1(c). This stencil is a combination of the cross stencil and rhombus stencil. Next, we study some kinds of retrogression of this FD scheme.

(1) Case 1: $N = 1$

When $N = 1$, this FD scheme is reduced to the conventional cross-stencil-based FD scheme (Liu & Sen 2009), which can be expressed by

$$\frac{1}{h^2} \left[c_0 P_{0,0}^0 + \sum_{m=1}^M c_m (P_{-m,0}^0 + P_{m,0}^0 + P_{0,-m}^0 + P_{0,m}^0) \right] \approx \frac{1}{v^2 \tau^2} [-2P_{0,0}^0 + (P_{0,0}^{-1} + P_{0,0}^1)], \quad (7)$$

where, c_m are the FD coefficients. If c_m are derived from the spatial dispersion relation alone, this FD scheme is named as conventional space-domain FD scheme. By contrast, if c_m are derived from the time-space dispersion relation, this FD scheme is named as conventional time-space-domain FD scheme (Liu & Sen 2009). Eq. (7) is the FD scheme commonly used to solve 2-D constant-density acoustic wave equation.

(2) Case 2: $N = M$

When $N = M$, this FD scheme is reduced to the rhombus FD scheme (Liu & Sen 2013).

2.2 TE-based new time-space-domain FD schemes for 2-D acoustic wave equation

In the FD scheme introduced above, FD coefficients for spatial derivatives in eq. (2) and temporal derivatives in eq. (4) are derived independently based on their respective dispersion relations. If the FD coefficients are derived from the time-space-domain dispersion relation, the accuracy can be increased greatly (Liu & Sen 2009). Therefore, in this section, we derive the FD coefficients in the joint time-space domain using TE for our new FD scheme.

According to the plane wave theory, we have

$$P_{m,n}^I = e^{i[k_x(x+mh)+k_z(z+nh)-\omega(t+l\tau)]}, \quad (8)$$

where, $k_x = k \cos \theta$, $k_z = k \sin \theta$, k is the wavenumber, θ is the propagation angle, ω is the angular frequency and $i = \sqrt{-1}$.

Substituting eq. (8) into eq. (6) and simplifying it, the time-space-domain dispersion relation of the wave equation for our new FD scheme is

$$a_{0,0} + 2 \sum_{m=1}^M a_{m,0} [\cos(mk_x h) + \cos(mk_z h)] + 4 \sum_{m=1}^{N-1} \sum_{n=1}^{N-m} a_{m,n} [\cos(mk_x h) \cos(nk_z h)] \approx \frac{h^2}{v^2 \tau^2} [-2 + 2 \cos(\omega \tau)]. \quad (9)$$

Expanding the cosine functions of eq. (9) into Taylor series, we have

$$a_{0,0} + 2 \sum_{m=1}^M a_{m,0} \left[\sum_{j=0}^{\infty} \frac{(-1)^j m^{2j} (k_x^{2j} + k_z^{2j}) h^{2j}}{(2j)!} \right] + 4 \sum_{m=1}^{N-1} \sum_{n=1}^{N-m} \left[a_{m,n} \sum_{\varepsilon=0}^{\infty} \sum_{\xi=0}^{\infty} \frac{(-1)^{\varepsilon+\xi} m^{2\varepsilon} n^{2\xi}}{(2\varepsilon)!(2\xi)!} k_x^{2\varepsilon} k_z^{2\xi} h^{2\varepsilon+2\xi} \right] \approx 2 \sum_{j=1}^{\infty} \frac{(-1)^j r^{2j-2} (kh)^{2j}}{(2j)!}, \quad (10)$$

where, r is the Courant number, v is the phase velocity, and they satisfy $r = v\tau/h$, $v = \omega/k$.

Using

$$k^{2j} = (k_x^2 + k_z^2)^j = \sum_{\xi=0}^j \frac{j!}{\xi!(j-\xi)!} k_x^{2j-2\xi} k_z^{2\xi}, \quad (11)$$

eq. (10) can be written as

$$\begin{aligned} a_{0,0} + 4 \sum_{m=1}^M a_{m,0} + 4 \sum_{m=1}^{N-1} \sum_{n=1}^{N-m} a_{m,n} + 2 \sum_{m=1}^M a_{m,0} & \left[\sum_{j=1}^{\infty} \frac{(-1)^j m^{2j} (k_x^{2j} + k_z^{2j}) h^{2j}}{(2j)!} \right] \\ & + 4 \sum_{m=1}^{N-1} \sum_{n=1}^{N-m} a_{m,n} \left[\sum_{j=1}^{\infty} \frac{(-1)^j (m^{2j} k_x^{2j} + n^{2j} k_z^{2j}) h^{2j}}{(2j)!} + \sum_{\varsigma=1}^{\infty} \sum_{\xi=1}^{\infty} \frac{(-1)^{\varsigma+\xi} m^{2\varsigma} n^{2\xi} k_x^{2\varsigma} k_z^{2\xi} h^{2\varsigma+2\xi}}{(2\varsigma)!(2\xi)!} \right] \\ & \approx 2 \sum_{j=1}^{\infty} \left[\frac{(-1)^j r^{2j-2} (k_x^{2j} + k_z^{2j})}{(2j)!} \right] h^{2j} + 2 \sum_{j=1}^{\infty} \sum_{\xi=1}^{j-1} \left[\frac{(-1)^j r^{2j-2} k_x^{2j-2\xi} k_z^{2\xi} (j)!}{(2j)!(\xi)!(j-\xi)!} \right] h^{2j}. \end{aligned} \quad (12)$$

Comparing the polynomials coefficients of h^0 and h^{2j} ($j > 0$) on both sides of eq. (12), we obtain

$$a_{0,0} + 4 \sum_{m=1}^M a_{m,0} + 4 \sum_{m=1}^{N-1} \sum_{n=1}^{N-m} a_{m,n} = 0, \quad (13a)$$

$$\begin{aligned} \sum_{m=1}^M a_{m,0} \frac{(-1)^j m^{2j} (k_x^{2j} + k_z^{2j})}{(2j)!} + 2 \sum_{m=1}^{N-1} \sum_{n=1}^{N-m} a_{m,n} & \left[\frac{(-1)^j (m^{2j} k_x^{2j} + n^{2j} k_z^{2j})}{(2j)!} + \sum_{\xi=1}^{j-1} \frac{(-1)^j m^{2j-2\xi} n^{2\xi} k_x^{2j-2\xi} k_z^{2\xi}}{(2j-2\xi)!(2\xi)!} \right] \\ & \approx \left[\frac{(-1)^j r^{2j-2} (k_x^{2j} + k_z^{2j})}{(2j)!} \right] + \sum_{\xi=1}^{j-1} \left[\frac{(-1)^j r^{2j-2} k_x^{2j-2\xi} k_z^{2\xi} (j)!}{(2j)!(\xi)!(j-\xi)!} \right]. \end{aligned} \quad (13b)$$

Comparing the coefficients of $k_x^{2j-2\xi} k_z^{2\xi}$ on both sides of eq. (13b) leads to the following equations:

$$\sum_{m=1}^M m^{2j} a_{m,0} + 2 \sum_{m=1}^{N-1} \sum_{n=1}^{N-m} m^{2j} a_{m,n} = r^{2j-2} \quad (\xi = 0), \quad (14a)$$

$$\sum_{m=1}^M m^{2j} a_{m,0} + 2 \sum_{m=1}^{N-1} \sum_{n=1}^{N-m} n^{2j} a_{m,n} = r^{2j-2} \quad (\xi = j), \quad (14b)$$

$$2 \sum_{m=1}^{N-1} \sum_{n=1}^{N-m} \frac{m^{2j-2\xi} n^{2\xi}}{(2j-2\xi)!(2\xi)!} a_{m,n} = \frac{j! r^{2j-2}}{(2j)!\xi!(j-\xi)!} \quad (\xi = 1, 2, \dots, j-1). \quad (14c)$$

Considering the symmetry, that is, $a_{m,n} = a_{n,m}$, eqs (14) can be reduced as

$$\sum_{m=1}^M m^{2j} a_{m,0} + 2 \sum_{m=1}^{N-1} \sum_{n=1}^{N-m} m^{2j} a_{m,n} = r^{2j-2}, \quad (15a)$$

$$2 \sum_{m=1}^{N-1} \sum_{n=1}^{N-m} \frac{m^{2j-2\xi} n^{2\xi}}{(2j-2\xi)!(2\xi)!} a_{m,n} = \frac{j! r^{2j-2}}{(2j)!\xi!(j-\xi)!} \quad (\xi = 1, 2, \dots, \text{int}(j/2)). \quad (15b)$$

Eq. (15b) suggests that for a specific j , there are totally $\text{int}(j/2)$ independent equations. Therefore, if j ranges from 1 to N , the total number of the independent equations in eq. (15b) is $N^2/4$ when N is even or $(N^2 - 1)/4$ when N is odd. Moreover, supposing j ranges from 1 to M in eq. (15a), the number of the independent equations in eq. (15a) is M . Summing them up, the total number becomes $M + (N^2 - 1)/4$ when N is odd or $M + N^2/4$ when N is even. This number is identical to that of the independent FD coefficients in eqs (15). Therefore, the FD coefficients can be obtained by solving eqs (15) with j ranging from 1 to M in eq. (15a) and 1 to N in eq. (15b). It is worthwhile to note that N should be smaller than or equal to M in this new time-space-domain FD scheme.

Unlike conventional FD schemes, our new scheme can achieve $(2N)$ th-order modelling accuracy along all directions when eqs (15) and (13a) are used to solve the FD coefficients. This is demonstrated in Appendix. Next, we examine some special cases of eqs (15).

(1) Case 1: $N = M$

When $N = M$, eqs (15) are identical to that of the rhombus time–space-domain FD scheme (Liu & Sen 2013).

(2) Case 2: $N = 1$

If $N = 1$, eq. (15b) disappears and eq. (15a) is reduced as

$$\sum_{m=1}^M m^{2j} a_{m,0} = r^{2j-2} \quad (j = 1, 2, \dots, M). \quad (16)$$

Eq. (16) is the same as that of the conventional time–space-domain FD scheme under the condition of $\theta = 0^\circ$, because conventional time–space-domain FD scheme adopts the following equation to determine the FD coefficients (Liu & Sen 2009),

$$\sum_{m=1}^M m^{2j} (\cos^{2j} \theta + \sin^{2j} \theta) c_m = r^{2j-2} \quad (j = 1, 2, \dots, M). \quad (17)$$

In eq. (17), θ is usually set as $\pi/8$ so that the highest $(2M)$ th-order accuracy can be reached along eight directions in both time and space.

(3) Case 3: $r = 0$

If $r = 0$, eqs (15) are reduced as

$$\sum_{m=1}^M m^2 a_{m,0} = 1 \quad (j = 1), \quad (18a)$$

$$\sum_{m=1}^M m^{2j} a_{m,0} = 0 \quad (j = 2, \dots, M). \quad (18b)$$

Eqs (18) are actually identical to eqs (3), which are used to determine the FD coefficients in conventional space-domain FD scheme.

2.3 LS-based new time–space-domain FD schemes for 2-D acoustic wave equation

All new FD schemes, introduced above to compute their FD coefficients using TE, are prone to dispersion errors at relatively large wavenumber ranges. To increase the accuracy further for large wavenumbers in the new scheme, we apply the LS methods to determine the FD coefficients based on the time–space-domain dispersion relation in this section.

Using the relationships of $k_x = k \cos \theta$, $k_z = k \sin \theta$ and $\beta = kh$, the time–space-domain dispersion relation described in eq. (9) is changed as

$$\begin{aligned} & \sum_{m=1}^{N-1} \sum_{n=1}^{N-m} a_{m,n} [2 - \cos(m\beta \cos \theta + n\beta \sin \theta) - \cos(m\beta \cos \theta - n\beta \sin \theta)] + \sum_{m=1}^M a_{m,0} [2 - \cos(m\beta \cos \theta) - \cos(m\beta \sin \theta)] \\ & \approx r^{-2} [1 - \cos(r\beta)]. \end{aligned} \quad (19)$$

The relative error of phase velocity ξ is

$$\xi(\beta, \theta) = \frac{v_{\text{FD}}}{v} - 1 = \frac{2}{r\beta} \sin^{-1} \sqrt{\frac{r^2}{2} \sum_{m=1}^{M_0} d_m \varphi_m(\beta, \theta) r^{-2} (1 - \cos(r\beta))} - 1, \quad (20)$$

Table 1. Some abbreviations and their meanings.

Abbreviation	Meaning
C-TDSD-TEM	Conventional method adopting eq. (7) and determining FD coefficients using eq. (3).
C-TSD-TEM	Conventional method adopting eq. (7) and determining FD coefficients using eq. (17).
C-TSD-LSM	Conventional method adopting eq. (7) and determining FD coefficients using eq. (25) with $N = 1$.
N-TDSD-TEM	New method adopting eq. (6) and determining FD coefficients using eqs (5) and (3) with $N > 1$.
N-TSD-TEM	New method adopting eq. (6) and determining FD coefficients using eqs (15) and (13a) with $N > 1$.
N-TSD-LSM	New method adopting eq. (6) and determining FD coefficients using eqs (25) and (13a) with $N > 1$.

where, $M_0 = M + \text{int}(N^2/4)$, d_m represent one kind of arrangement of $a_{m,0}$ and $a_{m,n}$ in order to simplify eq. (20),

$$\varphi_m(\beta, \theta) = \begin{cases} \frac{(2 - \cos(m\beta \cos \theta) - \cos(m\beta \sin \theta))}{r^{-2}(1 - \cos(r\beta))}, & (m \leq M) \\ \frac{\left(2 - \cos(m_1\beta \cos \theta + m_2\beta \sin \theta)\right)}{r^{-2}(1 - \cos(r\beta))}, & (m > M, m_1 = m_2) \\ \frac{\left(4 - \cos(m_1\beta \cos \theta + m_2\beta \sin \theta)\right)}{r^{-2}(1 - \cos(r\beta))}, & (m > M, m_1 \neq m_2) \end{cases} \quad (21)$$

The relationships among m_1 , m_2 and m in eq. (21) are

$$m = M + (m_1 - 1)N - m_1(m_1 - 1) + m_2, \quad 1 \leq m_1 \leq \text{int}(N/2), \quad m_1 \leq m_2 \leq N - m_1. \quad (22)$$

Optimal FD coefficients can be derived by minimizing the square error of time–space-domain dispersion relation over a given wavenumber range as follows:

$$E = \int_0^b \int_0^{2\pi} \left(\sum_{m=1}^{M_0} d_m \varphi_m(\beta, \theta) - 1 \right)^2 d\theta d\beta, \quad (23)$$

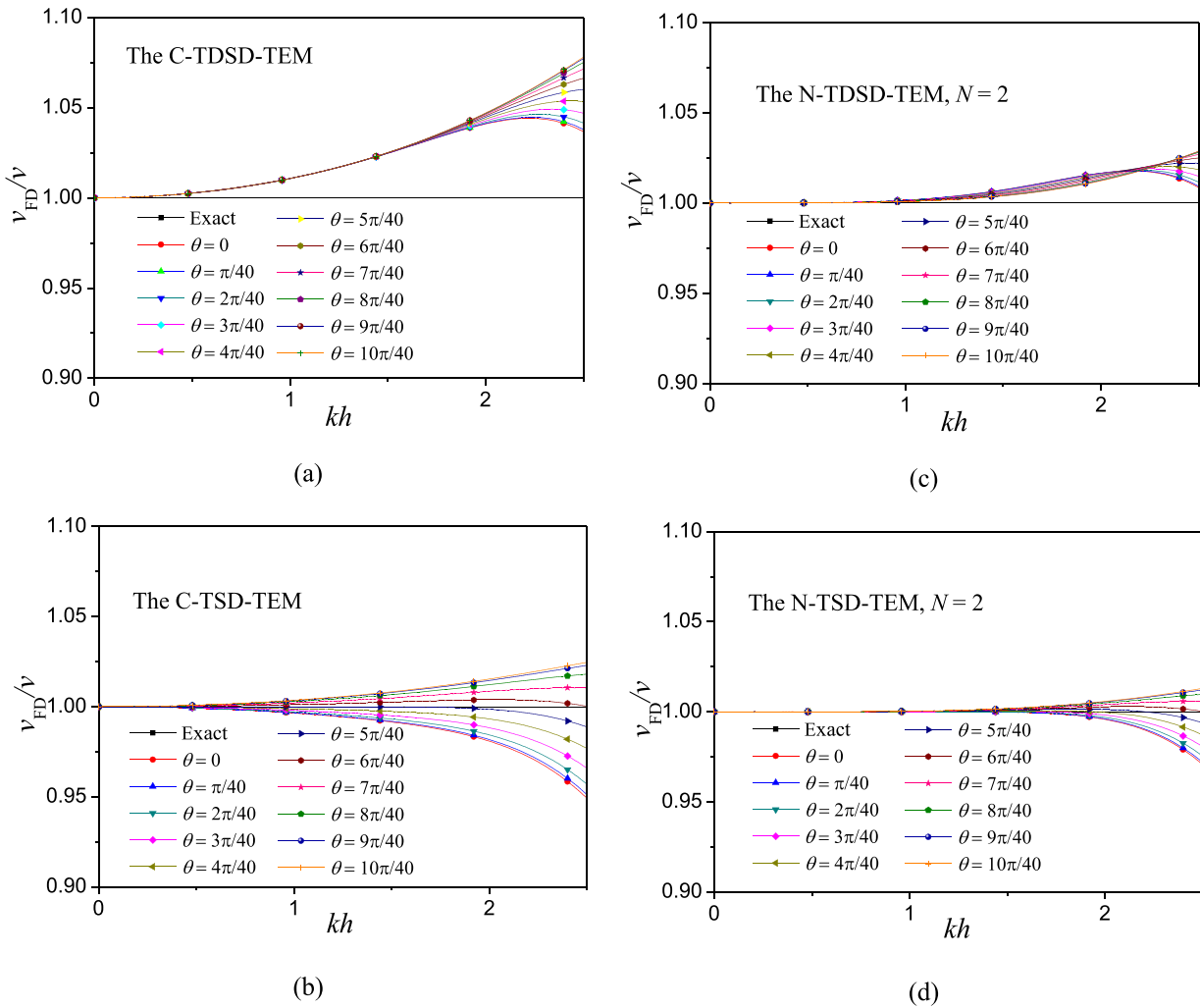


Figure 2. Phase velocity dispersion curves of C-TDSD-TEM, C-TSD-TEM, N-TDSD-TEM and N-TSD-TEM. $r = 0.5$, $M = 6$. (a) The C-TDSD-TEM. (b) The C-TSD-TEM. (c) The N-TDSD-TEM, $N = 2$. (d) The N-TSD-TEM, $N = 2$.

where, parameter b is the maximum wavenumber and it can be determined by the following equation

$$\xi_{\max} = \max_{\beta \in [0, b], \theta \in [0, \pi/4]} |\xi(\beta, \theta)| \leq \eta, \quad (24)$$

where, η is the given maximum allowed error. It is worthwhile to note that, the lower limit of the first integration in eq. (23) can be a given non-zero value because the zero frequency case sometimes is not relevant in many wave propagation applications. To balance the error over wider wavenumber range, here we simply set the lower limit to zero.

Because $\varphi_1(\beta), \varphi_2(\beta), \dots$, and $\varphi_m(\beta)$ are linearly independent, globally optimal d_m can be obtained by solving the following equations using the LS method:

$$\sum_{m=1}^{M_0} \left(\int_0^b \int_0^{2\pi} \varphi_m(\beta, \theta) \varphi_n(\beta, \theta) d\theta d\beta \right) d_m = \int_0^b \int_0^{2\pi} \varphi_n(\beta, \theta) d\theta d\beta, \quad (n = 1, 2, \dots, M_0), \quad (25)$$

which is obtained by differentiating eq. (23) with respect to d_m . Note that when $N = 1$, eq. (25) is reduced to that of the conventional time-space-domain scheme optimized using LS (Liu 2013). Eq. (25) together with eq. (24) can be used to solve the FD coefficients under the condition of the given maximum allowed error when LS method is applied.

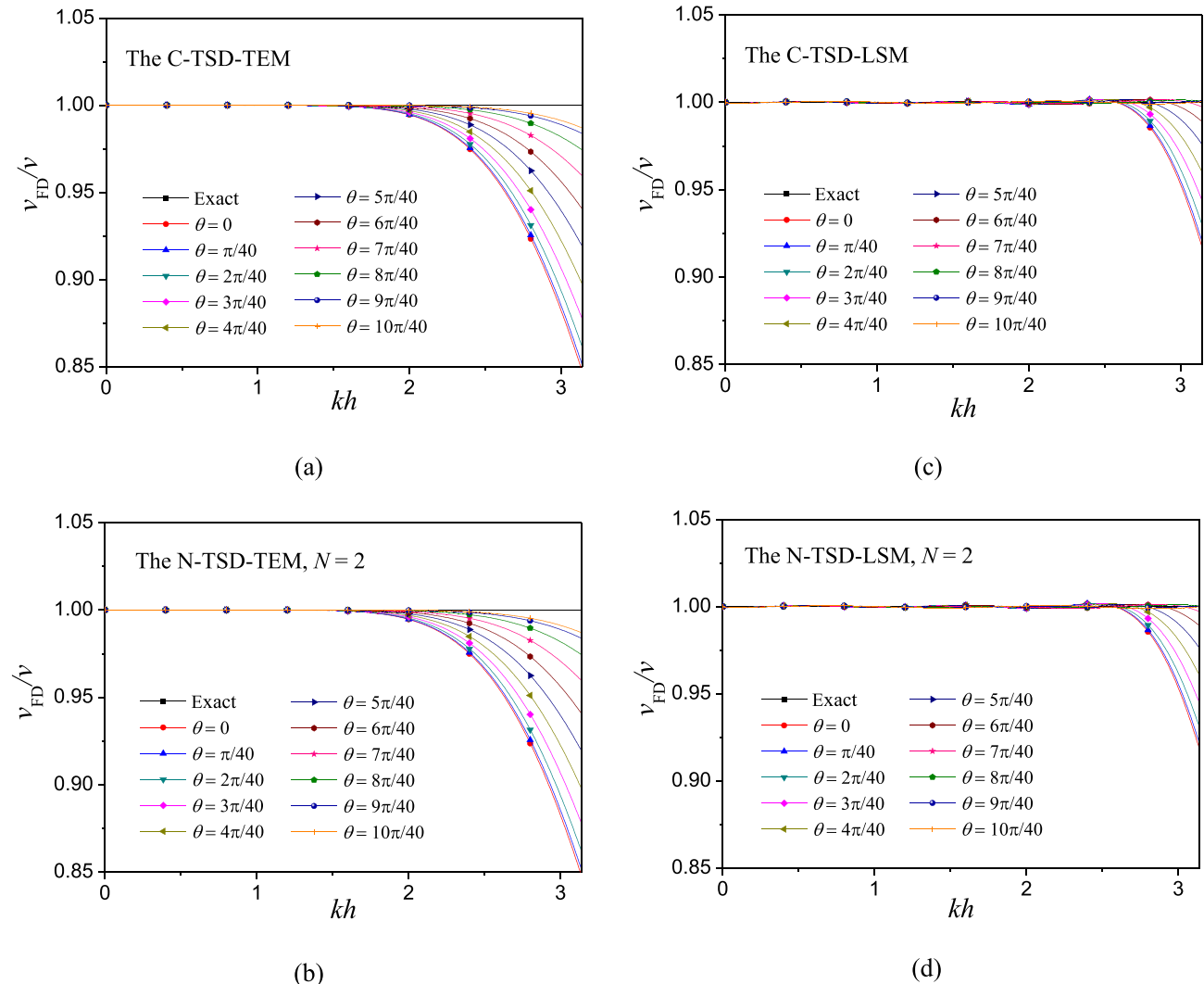


Figure 3. Phase velocity dispersion curves of the C-TSD-TEM, N-TSD-TEM, C-TSD-LSM and N-TSD-LSM using a small Courant number. $r = 0.05$, $M = 6$, $b = 2.74$ are used for both the C-TSD-LSM and N-TSD-LSM. (a) The C-TSD-TEM. (b) The N-TSD-TEM, $N = 2$. (c) The C-TSD-LSM. (d) The N-TSD-LSM, $N = 2$.

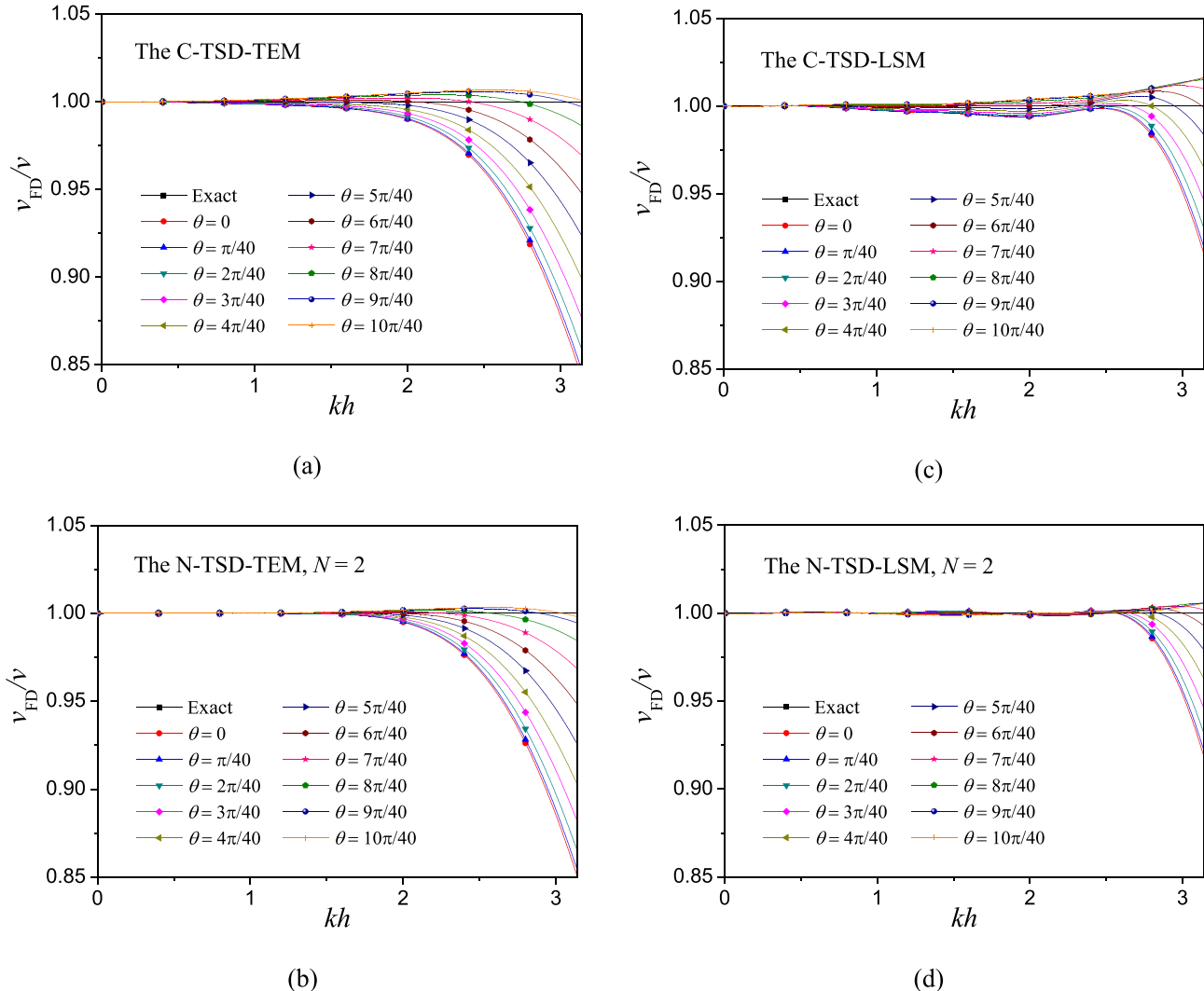


Figure 4. Phase velocity dispersion curves of the C-TSD-TEM, N-TSD-TEM, C-TSD-LSM and N-TSD-LSM using a middle Courant number. $r = 0.3$, $M = 6$, $b = 2.74$ are used for both the C-TSD-LSM and N-TSD-LSM. (a) The C-TSD-TEM. (b) The N-TSD-TEM, $N = 2$. (c) The C-TSD-LSM. (d) The N-TSD-LSM, $N = 2$.

3 DISPERSION ANALYSIS

In this section, we compare our new LS-based and TE-based FD schemes with conventional LS-based and TE-based FD schemes through dispersion analysis. For simplicity, we apply some abbreviations in the following. These abbreviations are listed in Table 1.

For conventional space-domain and time-space-domain FD schemes, that is, C-TDSD-TEM, C-TSD-TEM and C-TSD-LSM, we define a parameter δ_{PH} as follows, to describe 2-D phase velocity dispersion (Liu & Sen 2009),

$$\delta_{\text{PH}} = \frac{v_{\text{FD}}}{v} = \frac{2}{rkh} \sin^{-1} \sqrt{r^2 \sum_{m=1}^M c_m \left(\sin^2 \left(\frac{mkh \sin \theta}{2} \right) + \sin^2 \left(\frac{mkh \cos \theta}{2} \right) \right)}. \quad (26)$$

For our new schemes, that is, N-TDSD-TEM, N-TSD-TEM and N-TSD-LSM, δ_{PH} is defined as

$$\delta_{\text{PH}} = \frac{v_{\text{FD}}}{v} = \frac{2}{rkh} \sin^{-1} \sqrt{r^2 Q}, \quad (27)$$

where,

$$Q = \sum_{m=1}^M a_{m,0} \left[\sin^2 \left(\frac{mkh}{2} \cos \theta \right) + \sin^2 \left(\frac{mkh}{2} \sin \theta \right) \right] + \sum_{m=1}^{N-1} \sum_{n=1}^{N-m} a_{m,n} \left[\sin^2 \left(\frac{mkh \cos \theta + nkh \sin \theta}{2} \right) + \sin^2 \left(\frac{mkh \cos \theta - nkh \sin \theta}{2} \right) \right].$$

If δ_{PH} equals 1, no dispersion exists. If δ_{PH} is far from 1, FD scheme suffers from significant dispersion. Because kh equals π at the Nyquist frequency, kh only ranges from 0 to π when calculating δ_{PH} . Moreover, considering the periodicity of trigonometric function, we only compute δ_{PH} with θ ranging from 0° to 45° .

First, dispersion curves of C-TDSD-TEM, C-TSD-TEM, N-TDSD-TEM and N-TSD-TEM are compared to prove the accuracy improvement of our methods, as are displayed in Fig. 2. It is clear that, N-TDSD-TEM achieves higher accuracy and wider effective wavenumber ranges than both C-TDSD-TEM and C-TSD-TEM. Meanwhile, the N-TSD-TEM shows the smallest dispersion error. Fig. 2 proves that our new FD schemes are more accurate than conventional cross-stencil based schemes and time-space-domain dispersion relation is preferred over space-domain dispersion when determining FD coefficients. Therefore, in the following parts, only N-TSD-TEM is adopted for our new FD scheme when TE is used to determine the coefficients.

Next, we compare and analyse the dispersion curves of four kinds of FD methods using different Courant numbers. The variations of Courant numbers can reflect the variation of time step, supposing that fixed uniform grid spacing is adopted. This supposition is commonly true since uniform grid spacing is adopted for most modelling applications. Therefore, such comparison can help illustrate which scheme exhibits higher temporal accuracy indirectly. Figs 3–5 depict the corresponding phase velocity dispersion curves of these FD methods using small, middle and large Courant numbers respectively. We observe that, when the Courant number is small, all methods obtain very high accuracy. The similarities between Figs 3(a) and (b), and also Figs 3(c) and (d), demonstrate the correctness of our new FD schemes. Moreover, phase velocities dispersion error of C-TSD-LSM and N-TSD-LSM is smaller than that of C-TSD-TEM and N-TSD-TEM, which suggests that higher accuracy can be reached by using LS-based FD coefficients. When a larger Courant number 0.3 is adopted, dispersion

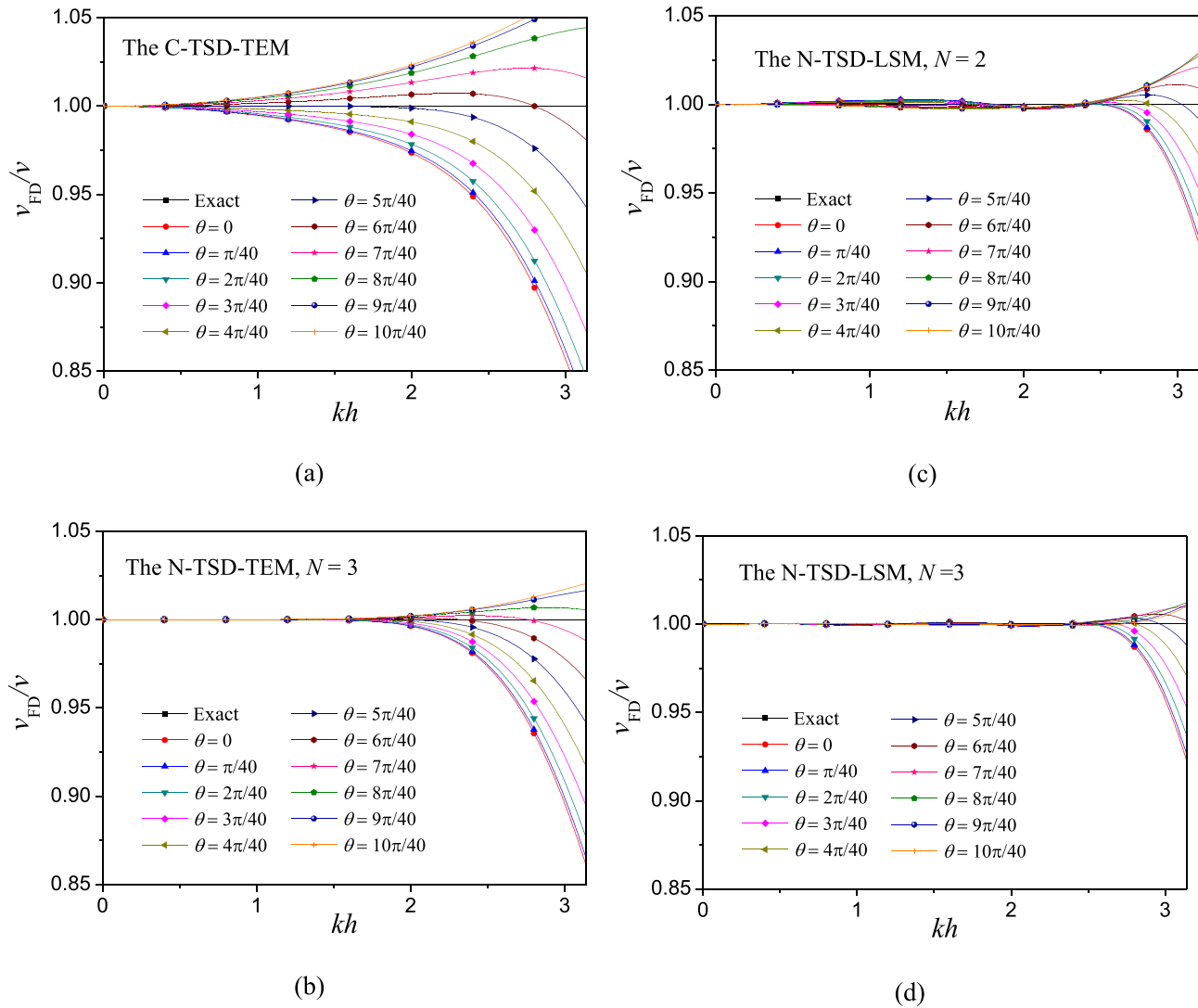


Figure 5. Phase velocity dispersion curves of the C-TSD-TEM, N-TSD-TEM and N-TSD-LSM using a large Courant number. $r = 0.6$, $M = 6$, $b = 2.74$ are used for the N-TSD-LSM method. C-TSD-LSM is not shown here because it is unstable. (a) The C-TSD-TEM. (b) The N-TSD-TEM, $N = 3$. (c) The N-TSD-LSM, $N = 2$. (d) The N-TSD-LSM, $N = 3$.

error for C-TSD-TEM increases obviously while it hardly changes for N-TSD-TEM, which suggests that N-TSD-TEM has higher temporal accuracy than C-TSD-TEM. For LS-based FD schemes, C-TSD-LSM exhibits obvious dispersion in Fig. 4(c) while our N-TSD-LSM keeps the dispersion error nearly same as that shown in Figs 3(c) and (d). If the Courant number is further increased to 0.6, the dispersion error for C-TSD-TEM is significant, and δ_{PH} is far from 1 even for small wavenumbers, as is indicated by Fig. 5(a). By contrast, the dispersion error for our N-TSD-TEM with $N = 3$, displayed in Fig. 5(b), is still well controlled and Fig. 5(b) is nearly same as Fig. 3(b). For the LS-based scheme, the C-TSD-LSM becomes unstable. However, our N-TSD-LSM is still stable, suggesting that N-TSD-LSM is more stable than C-TSD-LSM. Fig. 5(c) also suggests that N-TSD-LSM with $N = 2$ can achieve wider effective wavenumber range than C-TSD-TEM in Fig. 5(a) and N-TSD-TEM in Fig. 5(b). Moreover, comparison between Figs 5(c) and 4(d) demonstrates that the dispersion error slightly increases when r increases from 0.3 to 0.6. If N is increased from 2 to 3, this dispersion error is then decreased, which suggests that increasing N can decrease the dispersion error. We also compare the group velocity dispersion curves and observe that they show consistent characteristics as phase velocity dispersion curves. For simplification, we don't display them here.

Third, we conduct a comparison to further show the role of parameter N in our new FD scheme. Figs 6 and 7 depict the corresponding phase velocity dispersion curves of our N-TSD-TEM and N-TSD-LSM along 0° and 45° propagation directions. The involved parameters are described in the figure captions. It can be theoretically proved that when θ is 0° , the dispersion relation in eq. (27) is independent on operator length N and all the N-TSD-TEM have identical dispersion relation when TE is used to determine the coefficients. This explains why the five curves of N-TSD-TEM in Fig. 6(a) overlap with each other. Figs 6 and 7 suggest that, N-TSD-TEM has smaller dispersion error and wider effective wavenumber range than C-TSD-TEM. For N-TSD-TEM, increasing value of N improves the accuracy as well,

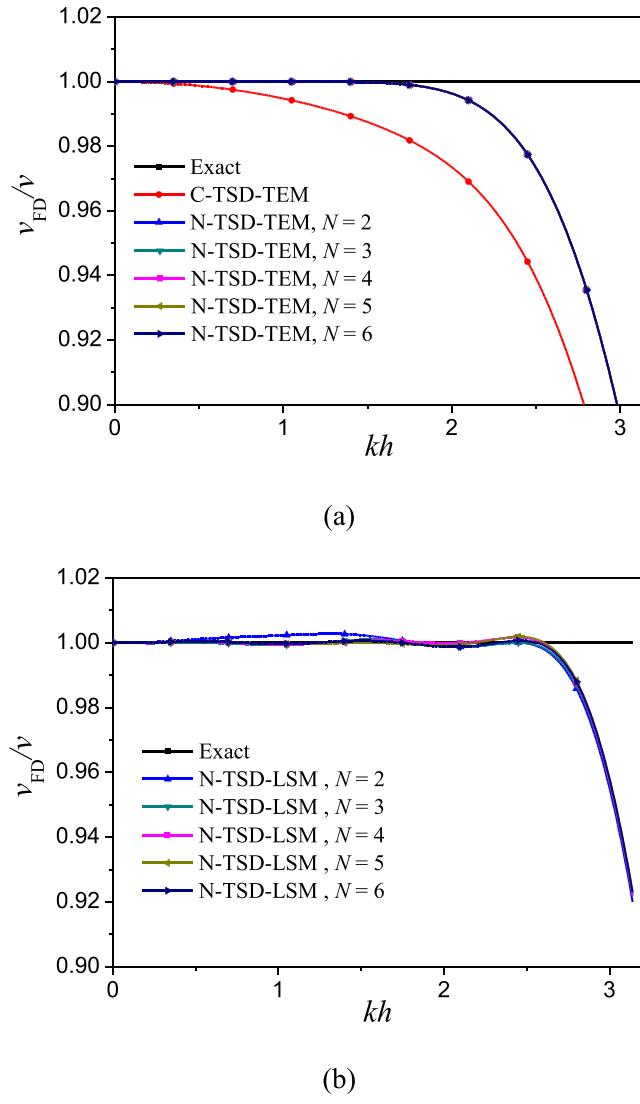


Figure 6. Comparisons of phase velocity dispersion curves computed by C-TSD-TEM, N-TSD-TEM and N-TSD-LSM along 0° propagation direction. $r = 0.6$, $M = 6$, $b = 2.74$ are used in the N-TSD-LSM. The C-TSD-LSM is unstable for the given parameters. (a) The C-TSD-TEM and N-TSD-TEM. (b) The N-TSD-LSM. Note that, the five curves corresponding to the N-TSD-TEM methods in (a) overlap with each other.

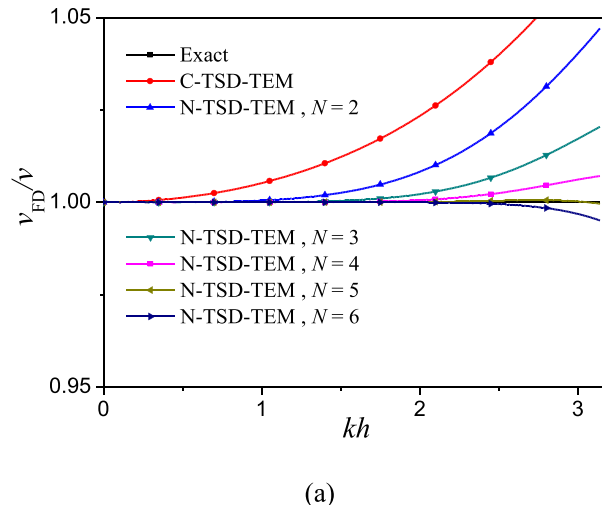
as is shown in Fig. 7(a). Moreover, LS-based FD schemes displayed in Figs 6(b) and 7(b) exhibit much wider wavenumber range than TE-based FD schemes displayed in Figs 6(a) and 7(a), thus they have higher accuracy. N-TSD-LSM with $N = 2$ or 3 can already achieve greater accuracy and increasing N from 3 to 6 improves the accuracy indistinctively. Moreover, the N-TSD-LSM is more stable than C-TSD-LSM.

In order to convincingly demonstrate the advantage of our new schemes in suppressing the temporal dispersion, we further compare the phase velocity dispersion curves of the aforementioned four kinds of FD methods using the same velocity and grid spacing. We investigate the variation of dispersion error with time step by using different time steps, as displayed in Fig. 8. Because of having demonstrated that accuracies of our N-TSD-TEM and N-TSD-LSM improve with the increase of N , we only show the curves of N-TSD-TEM and N-TSD-LSM with $M = N$ that exhibit the highest accuracy. From Fig. 8, we can conclude, C-TSD-TEM is prone to dispersion errors when time step is relatively large. The dispersion error increases significantly with time step for C-TSD-TEM. By contrast, the N-TSD-TEM maintains the accuracy well in Fig. 8(b). The same conclusion can be drawn for LS-based FD schemes shown in Figs 8(c) and (d). Besides, the C-TSD-LSM becomes unstable when time step equals 4 ms. However, N-TSD-LSM is still stable, suggesting that N-TSD-LSM is less stringent than C-TSD-LSM. Comparison of Fig. 8(b) with (d) also indicates that N-TSD-LSM is more accurate than N-TSD-TEM.

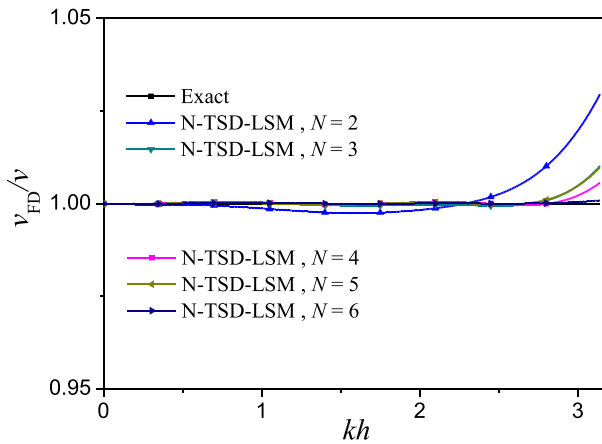
4 STABILITY ANALYSIS

Using the conventional eigenvalue method of stability analysis, the stability condition for both C-TSD-TEM and C-TSD-TEM (Liu & Sen 2009) is expressed as

$$r \leq \left(\sum_{m=1}^M c_m ((-1)^{m-1} + 1) \right)^{-1/2}. \quad (28)$$



(a)



(b)

Figure 7. Same as Fig. 6 but along 45° propagation direction. (a) The C-TSD-TEM and N-TSD-TEM. (b) The N-TSD-LSM.

For our N-TSD-TEM and N-TSD-LSM (Liu & Sen 2013), the stability condition is

$$r \leq \left(\sum_{m=1}^M a_{m,0} ((-1)^{m-1} + 1) + \sum_{m=1}^{N-1} \sum_{n=1}^{N-m} a_{m,n} ((-1)^{m+n-1} + 1) \right)^{-1/2}. \quad (29)$$

We define the stability factor for C-TDSD-TEM and C-TSD-TEM as follows:

$$s = \left(\sum_{m=1}^M c_m ((-1)^{m-1} + 1) \right)^{-1/2}. \quad (30)$$

For N-TSD-TEM and N-TSD-LSM, the stability factor is defined as

$$s = \left(\sum_{m=1}^M a_{m,0} ((-1)^{m-1} + 1) + \sum_{m=1}^{N-1} \sum_{n=1}^{N-m} a_{m,n} ((-1)^{m+n-1} + 1) \right)^{-1/2}. \quad (31)$$

Fig. 9 displays the variation of the stability factors with operator length M for C-TDSD-TEM, C-TSD-TEM and N-TSD-TEM. The stability factor displayed here is the maximum allowed value of s satisfying $r \leq s$. This figure demonstrates that, the C-TDSD-TEM has the smallest stability factor, which suggests that it is easier to get unstable. Also, our N-TSD-TEM is less stringent than C-TSD-TEM because its

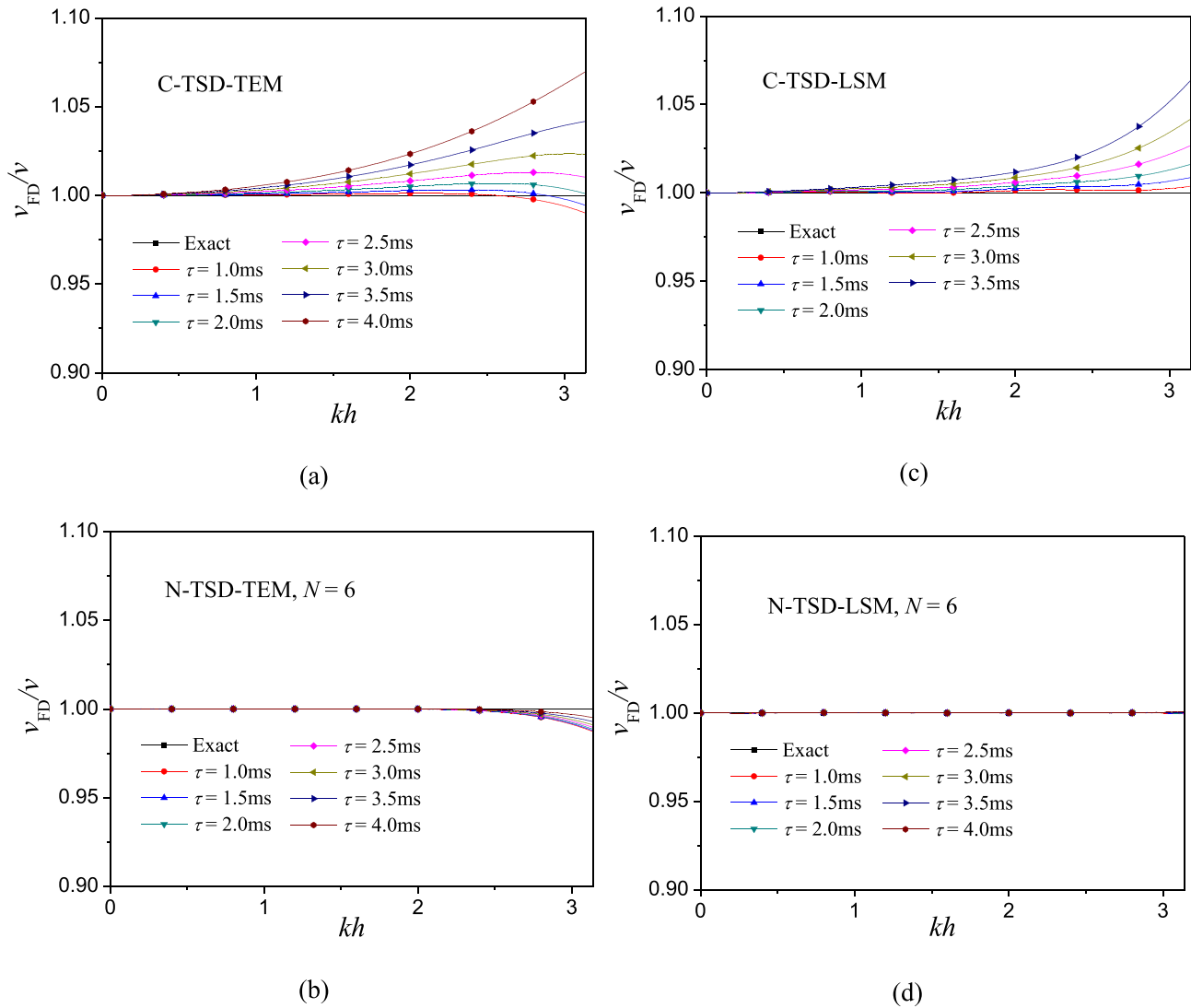


Figure 8. Comparisons of the phase velocity dispersion curves along 45° propagation direction with different time steps. $M = 6$, $h = 10$ m, $v = 1500$ m s^{-1} , $b = 2.74$ are used in the C-TSD-LSM and N-TSD-LSM methods. C-TSD-LSM is unstable when time step equals 4 ms. (a) The C-TSD-TEM. (b) The N-TSD-TEM, $N = 6$. (c) The C-TSD-LSM. (d) The N-TSD-LSM, $N = 6$.

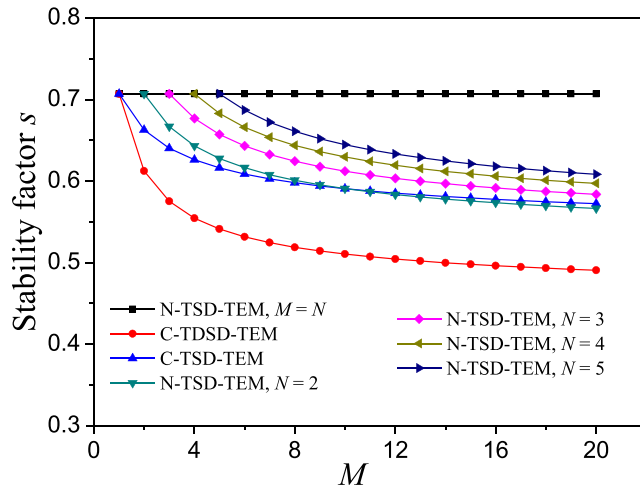


Figure 9. Variation of the stability factors with operator length M for C-TDSD-TEM, C-TSD-TEM and N-TSD-TEM. The method is stable when $r \leq s$.

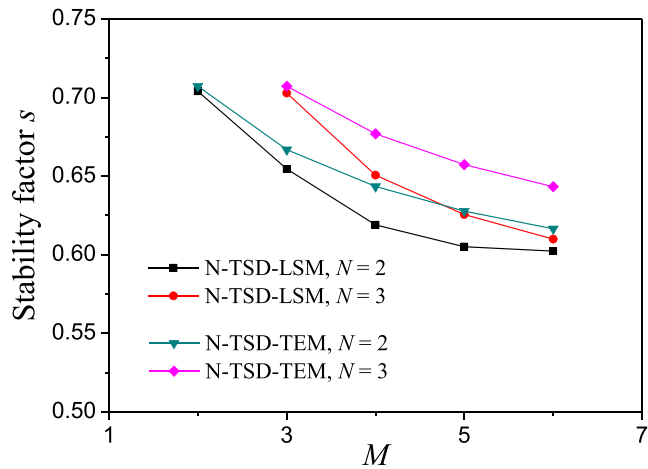


Figure 10. Comparisons of stability factors between N-TSD-TEM and N-TSD-LSM. The method is stable when $r \leq s$. $\eta = 10^{-2.5} \approx 0.003$ is used in the N-TSD-LSM methods.

stability factor is larger than that of C-TSD-TEM. Moreover, the stability factor for our N-TSD-TEM increases with the increase of parameter N , suggesting that the stability condition is improved. Particularly, when the TE-based rhombus time–space-domain FD scheme is used, the stability factor is always 0.707. This consists with the conclusion drawn in Liu & Sen (2013). Our new scheme thus can adopt larger time steps than conventional scheme.

We also compare the stability condition of N-TSD-LSM with that of the N-TSD-TEM, as is illustrated in Fig. 10. It is obvious that, stability conditions of the N-TSD-LSM are stricter than that of the N-TSD-TEM. In addition, stability factor increases with the increase of parameter N for N-TSD-LSM as well.

5 MODELLING EXAMPLES

In this section, we employ our N-TSD-TEM and N-TSD-LSM to perform numerical modelling on homogenous model, two-layer model and inhomogeneous model, and compare the modelling results with those of C-TSD-TEM, C-TSD-LSM and reference solution. To reduce the computational cost for modelling inhomogeneous models, we adopt the so-called adaptive variable length spatial operator scheme (Liu & Sen 2011), which uses long FD operators in regions of low velocity and short FD operators in regions of high velocity to reach the same modelling accuracy. According to Liu & Sen (2011), minimum values of operator length parameter M can be determined for different velocities by satisfying the following inequality for the given maximum frequency f_{\max} and maximum error η ,

$$|\varepsilon(v, M, f)| \leq \eta \text{ when } f \leq f_{\max}, \quad (32)$$

where, $\varepsilon = hv^{-1}(\delta_{\text{PH}}^{-1} - 1)$.

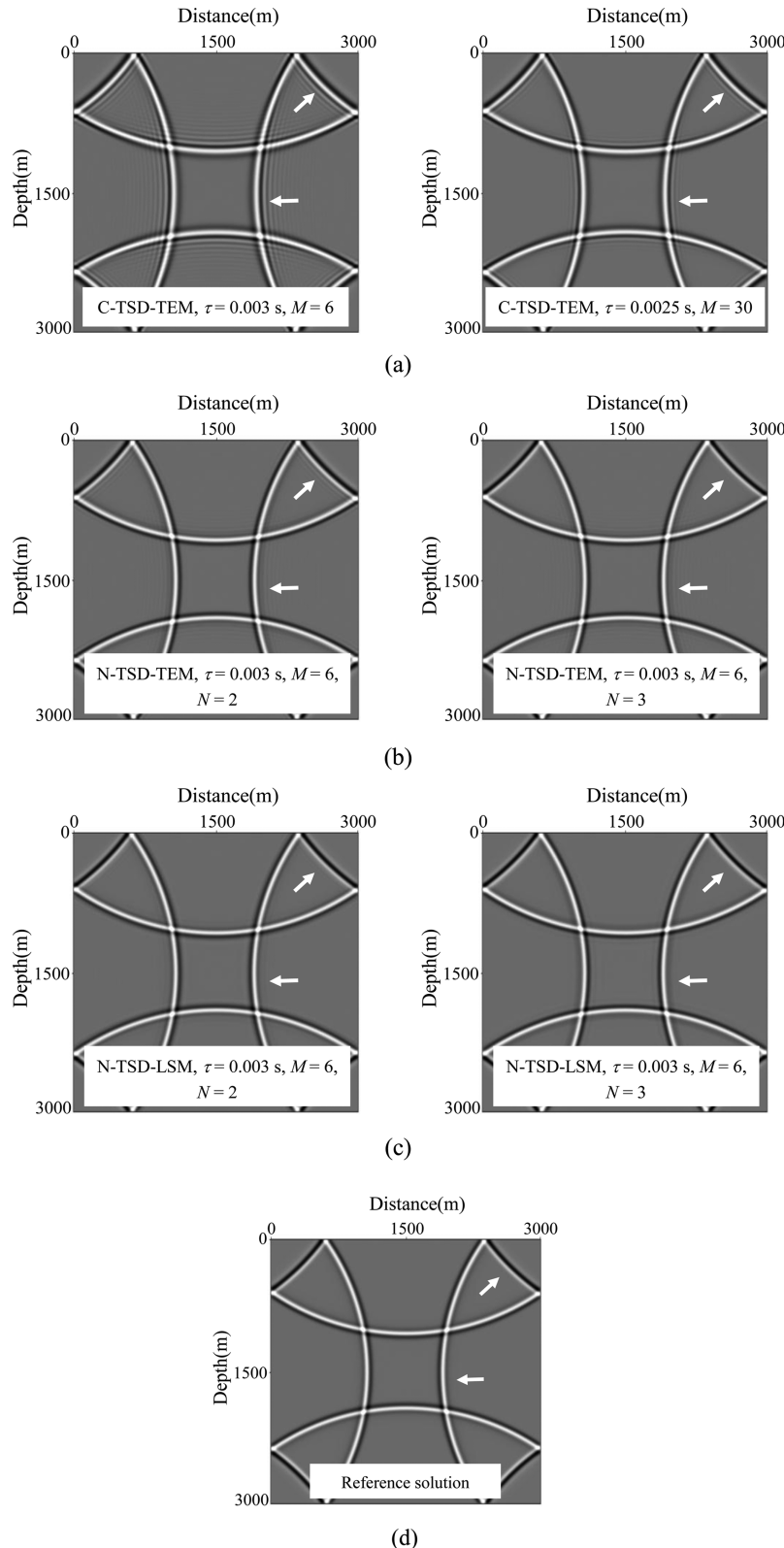


Figure 11. Snapshots of a homogeneous model at 900 ms. The model size is $3000 \text{ m} \times 3000 \text{ m}$. $\tau = 0.003 \text{ s}$, $h = 15 \text{ m}$, $v = 3000 \text{ m s}^{-1}$. The source located in the model centre is a Ricker-type wavelet with dominant frequency of 30 Hz. No ABCs are used. $\eta = 10^{-2.5} \approx 0.003$ is used in the LS-based schemes. C-TSD-LSM is unstable for the given parameters. C-TSD-TEM with $\tau = 0.003 \text{ s}$ and $M = 30$ is unstable as well, therefore, a smaller time step $\tau = 0.0025 \text{ s}$ is used instead. (a) The C-TSD-TEM with $\tau = 0.003 \text{ s}$, $M = 6$ (left) and $\tau = 0.0025 \text{ s}$, $M = 30$ (right). (b) The N-TSD-TEM with $N = 2$ (left) and $N = 3$ (right), $M = 6$. (c) The N-TSD-LSM with $N = 2$ (left) and $N = 3$ (right), $M = 6$. (d) Reference solution.

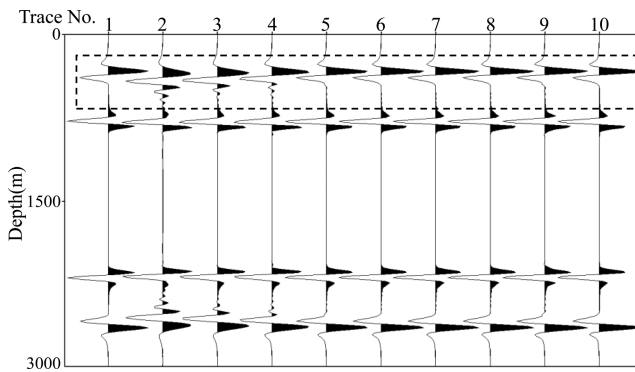


Figure 12. Comparisons of traces extracted from the snapshots at 900 ms computed by C-TSD-TEM, N-TSD-TEM and N-TSD-LSM, respectively. The value of x coordinate of each trace is 2700 m. Trace 1 is the reference solution selected from Fig. 11(d). Traces 2 and 3 are extracted from Fig. 11(a) with $M = 6$ and $M = 30$, respectively. Traces 4, 5, 6, 7 and 8 are computed by N-TSD-TEM with $N = 2, 3, 4, 5$ and 6 respectively. Traces 9 and 10 are computed by N-TSD-LSM with $N = 2$ and 3.

The first example is for a homogenous model. Modelling snapshots are displayed in Fig. 11. The related parameters are listed in the figure caption. The reference solution displayed in Fig. 11(d) is computed using C-TSD-TEM with a large operator length and a small time step. It is evident that the N-TSD-LSM provides the best simulated snapshots with the smallest dispersion, which can be illustrated by Fig. 11(c). The horizontal and tilted arrows in Fig. 11(a) indicate that C-TSD-TEM suffers from significant dispersion, even when a larger operator length and a smaller time step are used. Our N-TSD-TEM suppresses the dispersion to some extent. However, it still exists, which is indicated by the arrows in Fig. 11(b). Moreover, increasing parameter N in our N-TSD-TEM decreases the dispersion, because dispersion in Fig. 11(b), indicated by the tilted arrow, disappears when parameter N increases from 2 to 3. To show details of difference, we also show some traces ($x = 2700$ m) of the modelling snapshots in Fig. 12. Similar conclusions can be drawn.

The second example is for a two-layer model. Figs 13 and 14 show the snapshots computed using the aforementioned four kinds of FD schemes with two different time steps. The related parameters are displayed in the figure caption. We use C-TSD-TEM to produce reference solution with a large operator length and a small time step. Figs 13(a)–(c) suggest that, both C-TSD-TEM and N-TSD-TEM exhibit significant dispersion even when time step is 1 ms. By contrast, C-TSD-LSM and N-TSD-LSM yield satisfactory modelling results. However, if time step is increased to 2 ms, C-TSD-LSM becomes unstable. Therefore, we adopt $\tau = 1.6$ ms to conduct the modelling and the snapshot is displayed in Fig. 14(a). For N-TSD-LSM, $\tau = 2$ ms is still used. Fig. 14 suggests that C-TSD-LSM suffers from obvious dispersion, which is illustrated by the white arrow in Fig. 14(a), while our N-TSD-LSM produces satisfactory result. Note that the time step adopted by N-TSD-LSM is larger than that of the C-TSD-LSM, thus the N-TSD-LSM has higher accuracy and better stability than C-TSD-LSM. Also, variable spatial operator length method is stable for C-TSD-LSM when time step is 1 ms, as is displayed in Fig. 13(f), but it becomes unstable when time step increases to 2 ms. Using the same modelling parameters, however, variable spatial operator length method is still stable for our N-TSD-LSM, as is displayed in Fig. 14(c). Fig. 15 shows the waveforms at (300 m, 800 m) corresponding to the FD schemes used in Fig. 13. Similar conclusions can be drawn.

The third example is for the so-called 2-D Society of Exploration Geophysicists/European Association of Geoscientists and Engineers (SEG/EAGE) salt model depicted in Fig. 16. Hybrid ABCs (Liu & Sen 2010) are used for four boundaries with 10 grid points. The reference solution is computed by C-TSD-TEM using a very small time step and a large operator length. For C-TSD-TEM and N-TSD-TEM, we use the fixed operator length scheme, in which, the same spatial operator length is used for all the velocities. For C-TSD-LSM and N-TSD-LSM, we use the variable spatial operator length scheme. Figs 17 and 18 display the modelling snapshots and seismograms respectively. The arrows in Figs 17(b) and (c), and 18(b) and (c) indicated that both C-TSD-TEM and N-TSD-TEM using fixed spatial operator length methods suffer from significant dispersion even when time step equals 1 ms. However, both C-TSD-LSM and N-TSD-LSM using variable spatial operator length methods retain the waveform well. Fig. 19 displays the variations of FD operator lengths with velocities for C-TSD-TEM, N-TSD-TEM, C-TSD-LSM and N-TSD-LSM adopted in Figs 17 and 18. It suggests that C-TSD-LSM and N-TSD-LSM adopt much shorter FD operators than C-TSD-TEM and N-TSD-TEM and thus cost less computational time. Moreover, through increasing the values of parameter N from 1 to 3, time steps that equal 1 ms, 2 ms and 3 ms can be adopted by variable spatial operator length methods for C-TSD-LSM and N-TSD-LSM respectively. This can further reduce the computational cost. Fig. 20 displays the comparisons between the reference waveform and waveforms at (3600 m, 400 m) computed by the schemes mentioned above. Fig. 21 shows the corresponding globally normalized time-frequency envelope misfits. Here, the expression used for calculating misfit is taken from Kristekov'a *et al.* (2009; Table 1). It is evident that the C-TSD-LSM and N-TSD-LSM exhibit much smaller misfit than both C-TSD-TEM and N-TSD-TEM.

Table 2 displays the comparison of the CPU time consumed by seven different kinds of FD schemes under the condition of same maximum allowed dispersion error. To satisfy the same accuracy requirement, M should be at least 33 for C-TSD-TEM and 28 for our N-TSD-TEM respectively, if fixed operator length method is used. Using variable operator length schemes, spatial operator lengths are shortened significantly and thus the CPU time consumed decreases as well. It is worthwhile to note that, although N-TSD-TEM and N-TSD-LSM are

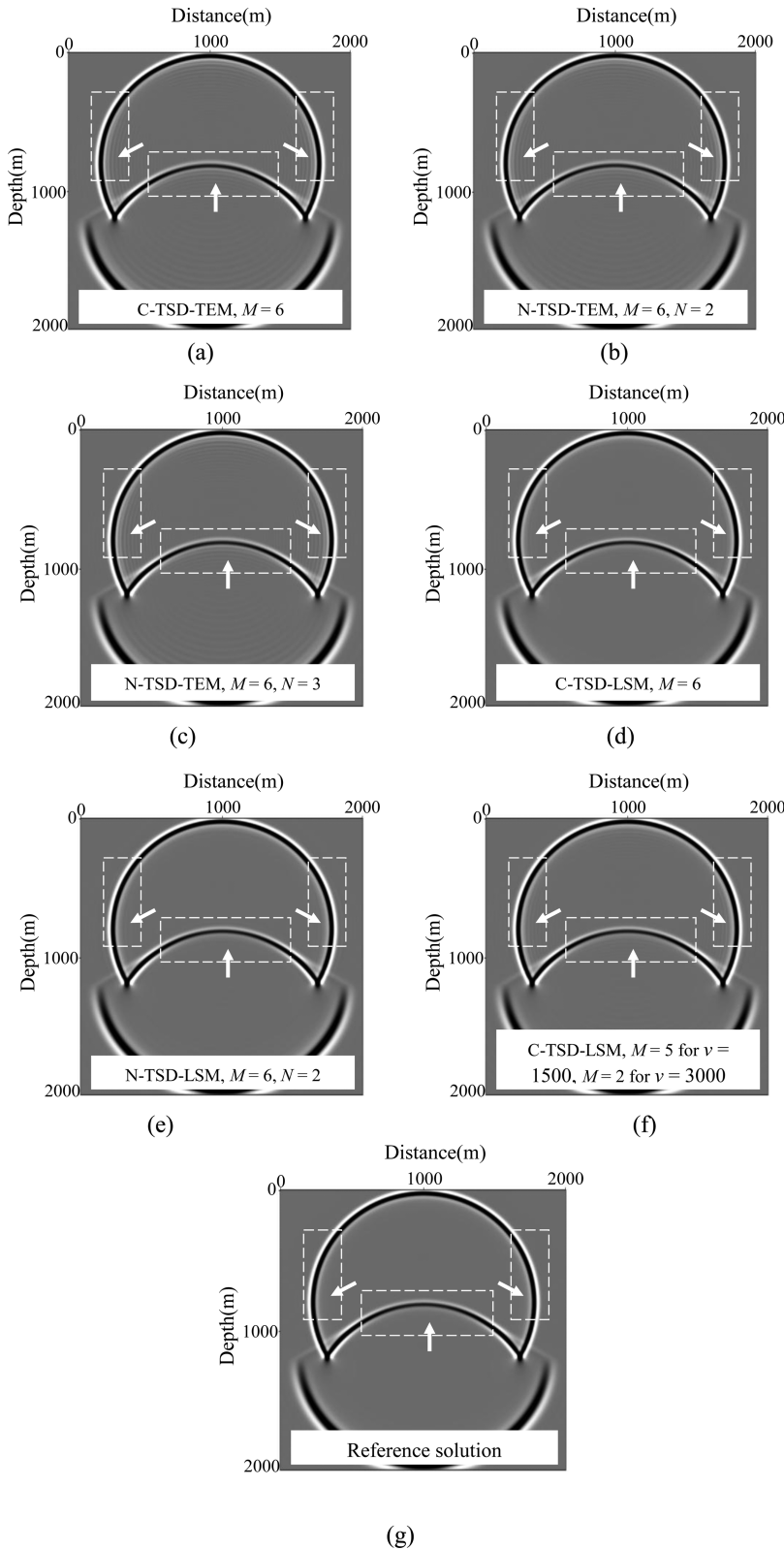


Figure 13. Snapshots at 560 ms for a two-layer model. The model size is 2000 m × 2000 m. $\tau = 0.001$ s, $h = 10$ m. $v = 1500$ m s $^{-1}$ for the upper layer and $v = 3000$ m s $^{-1}$ for the secondary layer. The interface depth is 1200 m. $\eta = 10^{-2.5} \approx 0.003$ is used in the C-TSD-LSM and N-TSD-LSM. For variable spatial operator length schemes, parameters $\eta = 10^{-5}$ and $f_{\max} = 50$ Hz are used. The source located at (1500 m, 800 m) is a Ricker-type wavelet with dominant frequency of 25 Hz. (a) The C-TSD-TEM, $M = 6$. (b) The N-TSD-TEM with $N = 2$, $M = 6$. (c) The N-TSD-TEM with $N = 3$, $M = 6$. (d) The C-TSD-LSM, $M = 6$. (e) The N-TSD-LSM with $N = 2$, $M = 6$. (f) The C-TSD-LSM with variable spatial operator length scheme, $M = 5$ for $v = 1500$ m s $^{-1}$ and $M = 2$ for $v = 3000$ m s $^{-1}$. (g) Reference solution.

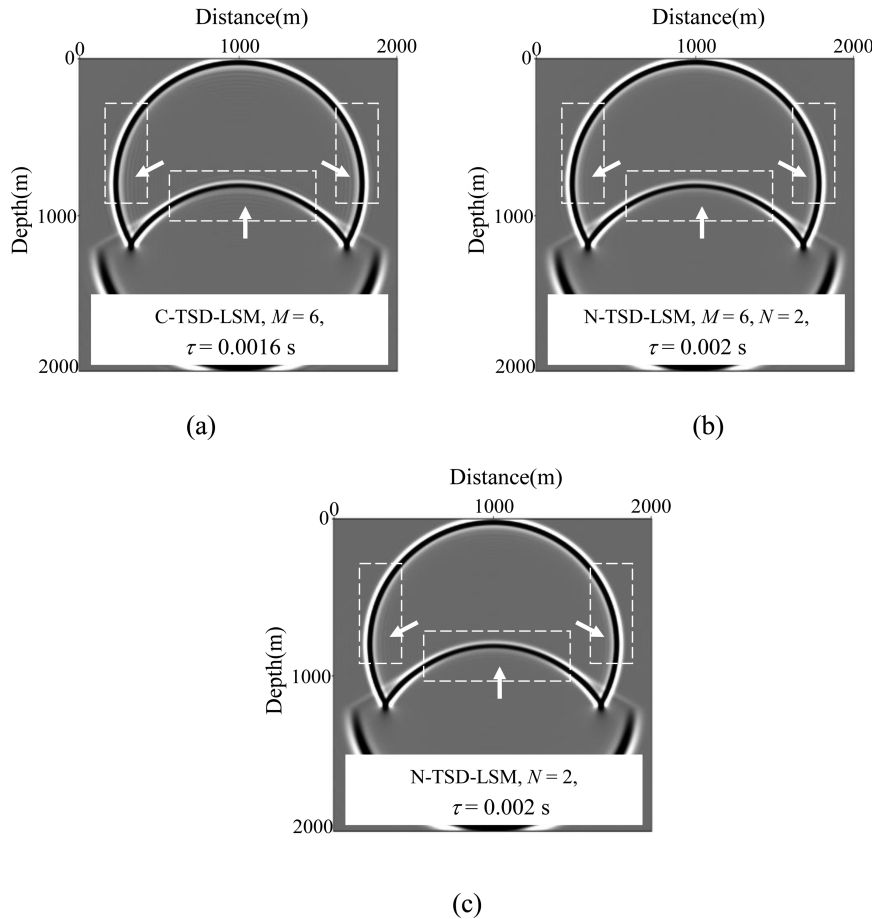


Figure 14. Snapshots at 560 ms for a two-layer model. The modelling parameters are all same to those that are described in the caption of Fig. 13 except using a relative large time step, $\tau = 0.002$ s. The C-TSD-LSM becomes unstable when $\tau = 0.002$ s is used, therefore, $\tau = 0.0016$ s is used instead in panel (a). (a) The C-TSD-LSM, $M = 6$, $\tau = 0.0016$ s. (b) The N-TSD-LSM with $N = 2$, $M = 6$, $\tau = 0.002$ s. (c) The N-TSD-LSM with variable spatial operator length scheme, $\tau = 0.002$ s, $N = 2$, $M = 6$ for $v = 1500 \text{ m s}^{-1}$ and $M = 2$ for $v = 3000 \text{ m s}^{-1}$.

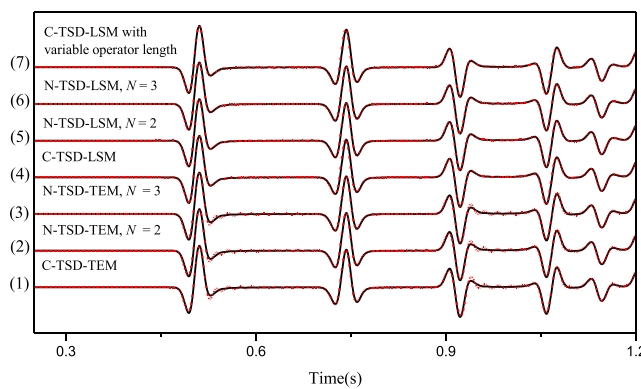


Figure 15. Comparisons between reference solution and calculated waveforms at (300 m, 800 m). The modelling parameters are same to those described in the caption of Fig. 13. From down to up, the comparisons are between the reference solution and the computed waveforms of (1) C-TSD-TEM, (2) N-TSD-TEM with $N = 2$, (3) N-TSD-TEM with $N = 3$, (4) C-TSD-LSM, (5) N-TSD-LSM with $N = 2$, (6) N-TSD-LSM with $N = 3$ and (7) C-TSD-LSM using variable operator length method respectively. The black solid line is the reference waveform and the red dashed line is the calculated waveform.

more computationally expensive than the C-TSD-TEM or the C-TSD-LSM for each time step, their overall computational cost is less. Because in C-TSD-TEM or C-TSD-LSM, a time step much smaller than the stability limit is often used to avoid the numerical dispersion, which results in large numbers of iteration time, whereas N-TSD-TEM and N-TSD-LSM can tolerate relatively larger time steps due to their high temporal accuracy. It is evident that, our N-TSD-LSM with $N = 3$ and $\tau = 3$ ms costs the least overall CPU time. The CPU time decreases from 434.420 s consumed by C-TSD-LSM to 175.334 s consumed by N-TSD-LSM, which is only 40 per cent of that of the C-TSD-LSM. Modelling efficiency is greatly increased by adopting our N-TSD-LSM using variable operator length schemes and large time steps.

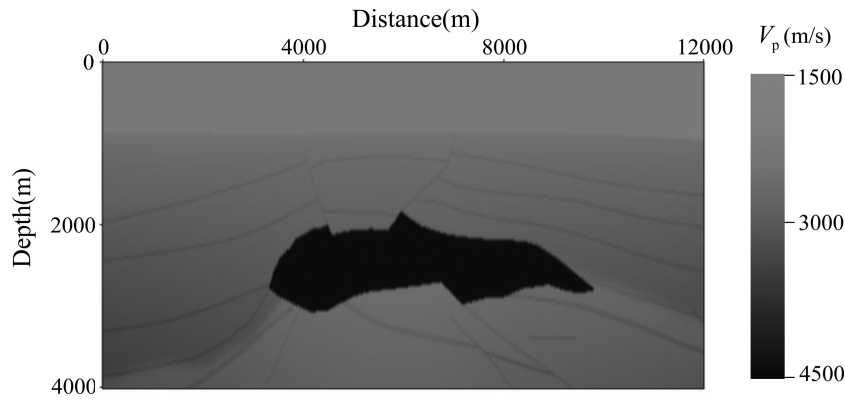


Figure 16. 2-D Society of Exploration Geophysicists/European Association of Geoscientists and Engineers (SEG/EAGE) salt model.

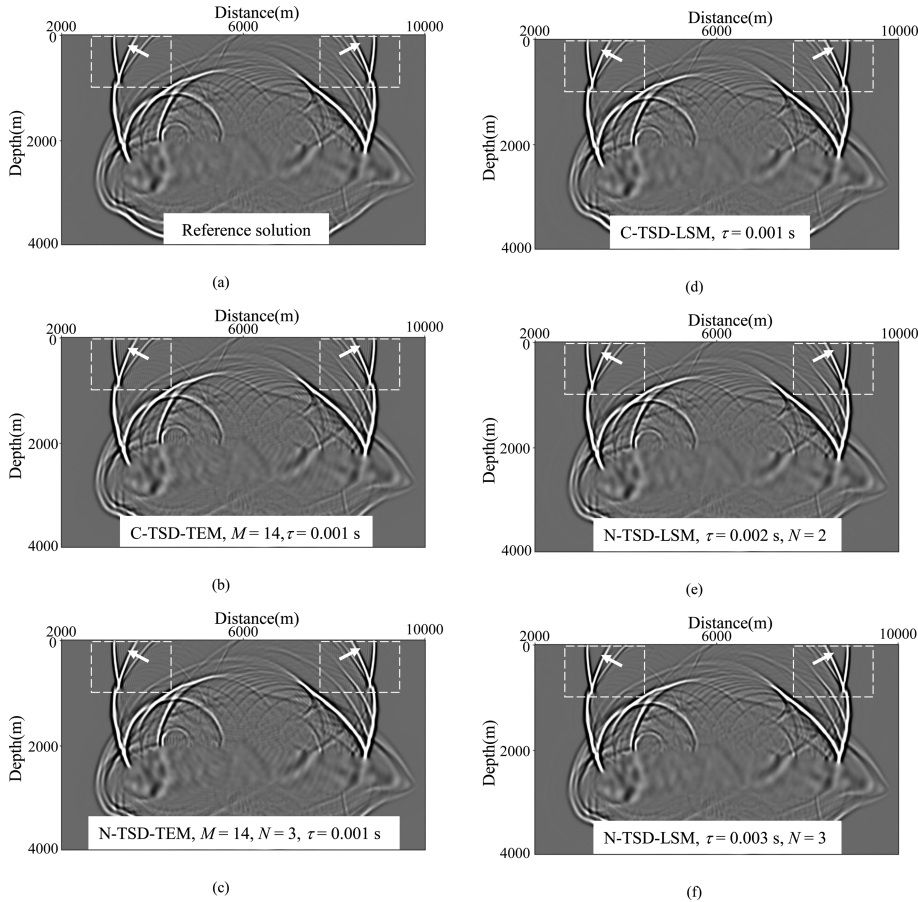


Figure 17. Snapshots at 1.98 s for the SEG/EAGE salt model. The model size is 12 000 m × 4000 m, $h = 20$ m. The source is located at (6000 m, 100 m). Receiver array is located at the same depth. The length of the recorded time is 6 s. A Ricker-type wavelet with dominant frequency of 15 Hz is used. $\eta = 10^{-5}$ and $f_{\max} = 34$ Hz are used in the variable spatial operator length schemes. (a) The reference solution computed by the C-TSD-TEM with a small time step and large M . (b) Snapshot computed by the C-TSD-TEM with $M = 14$ and $\tau = 0.001$ s. (c) Snapshot computed by the N-TSD-TEM with $M = 14$, $N = 3$ and $\tau = 0.001$ s. (d) Snapshot computed by the C-TSD-LSM using $\tau = 0.001$ s and variable spatial operator length method. M ranges from 2 to 14 for velocities ranging from 4481 to 1500 m s⁻¹. (e) Snapshot computed by the N-TSD-LSM using $\tau = 0.002$ s, $N = 2$ and variable spatial operator length method. M ranges from 2 to 14 for velocities ranging from 4481 to 1500 m s⁻¹. (f) Snapshot computed by the N-TSD-LSM using $\tau = 0.003$ s, $N = 3$ and variable spatial operator length method. M ranges from 3 to 14 for velocities ranging from 4481 to 1500 m s⁻¹.

6 DISCUSSIONS

In this section, we discuss two issues. One is to demonstrate which scheme exhibits the highest accuracy when the same number of grid points is involved. The other one is the simulation problem for models with large velocity contrast and large maximum velocity.

We discuss the first issue by comparing the accuracy of the conventional and new FD methods adopting stencils that involve the same number of grid points. The numbers of grid points involved in the cross stencil and new stencil are $4M + 1$ and $4M + 1 + 2N^2 - 2N$ respectively. Therefore, four kinds of stencils that contain the same 41 points are used here to discuss this issue. These four stencils are cross

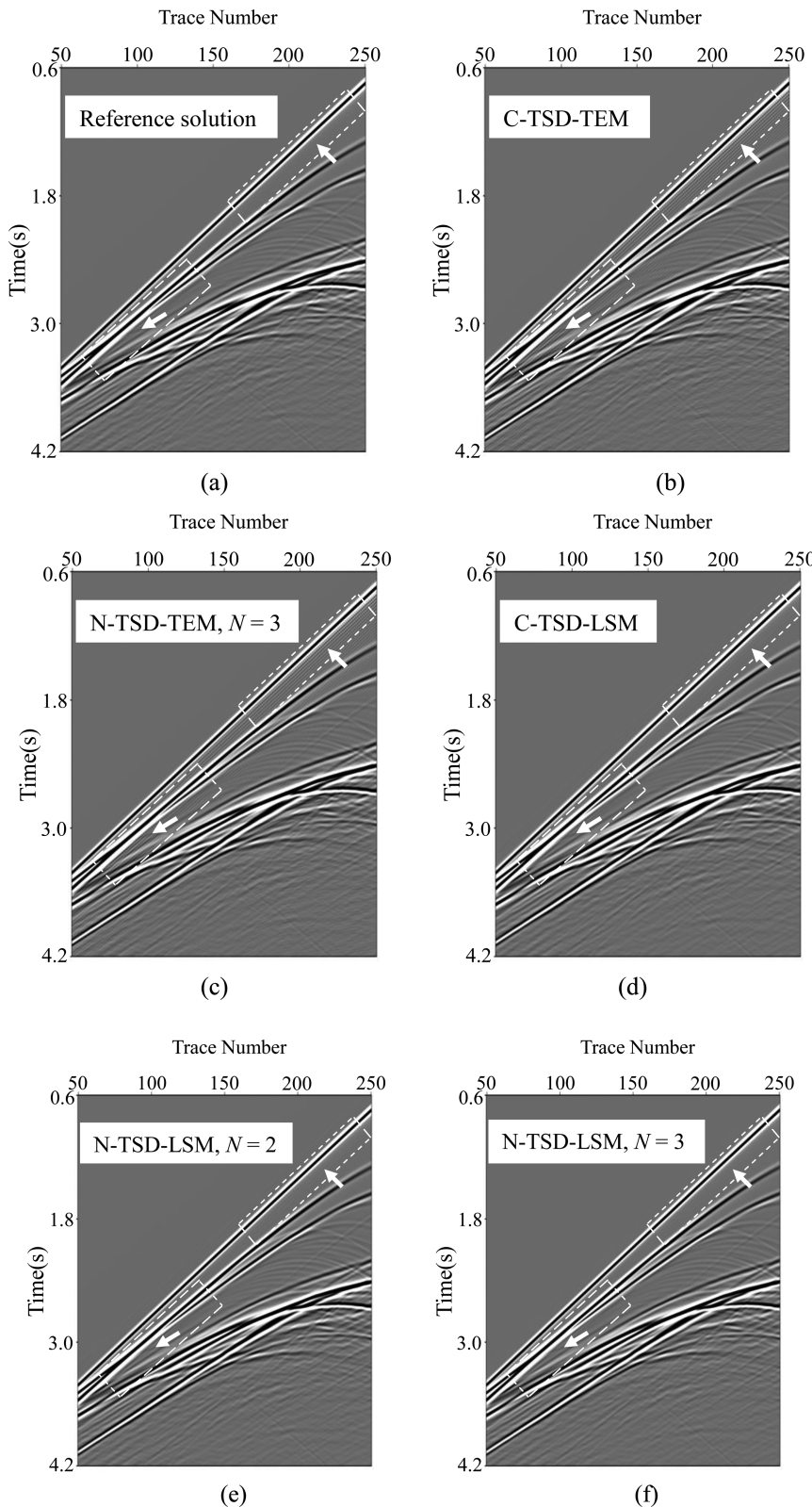


Figure 18. Records of the schemes in Fig. 17 for the SEG/EAGE salt model. (a) Reference solution. (b) The C-TSD-TEM. (c) The N-TSD-TEM, $N = 3$. (d) The C-TSD-LSM. (e) The N-TSD-LSM, $N = 2$. (f) The N-TSD-LSM, $N = 3$.

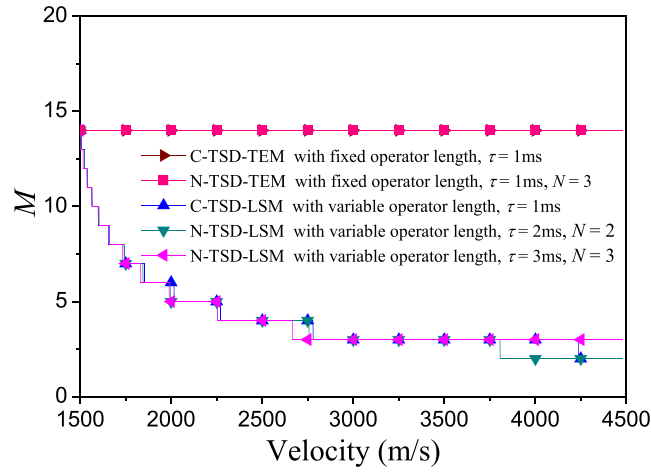


Figure 19. Variation of spatial operator lengths with velocities. For variable operator length schemes, $\eta = 10^{-5}$ and $f_{\max} = 34$ Hz are used.

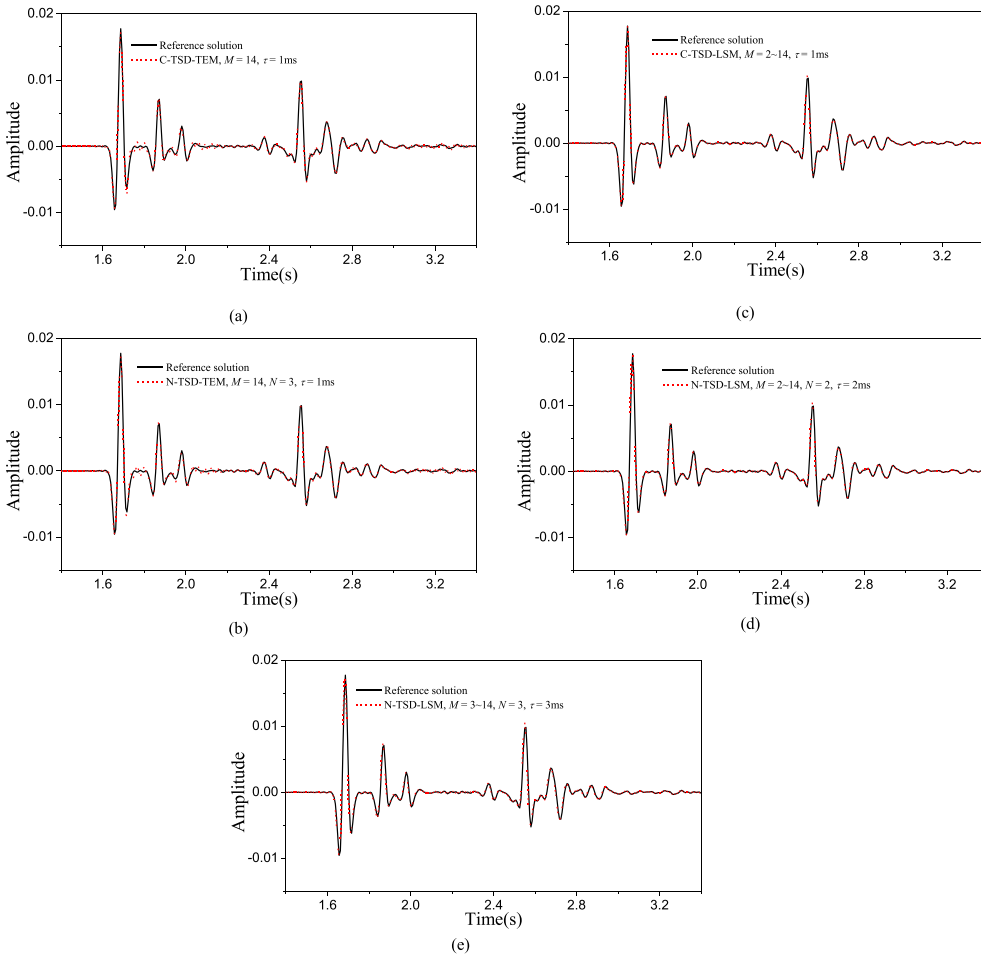


Figure 20. Comparison between the reference solution and waveforms computed by the schemes mentioned in the caption of Fig. 17 at (3600 m, 400 m). (a) The C-TSD-TEM. (b) The N-TSD-TEM with $N = 3$. (c) The C-TSD-LSM. (d) The N-TSD-LSM with $N = 2$. (e) The N-TSD-LSM with $N = 3$.

stencil using $M = 10$ denoted as (10, 1), our new stencil using $M = 9$ and $N = 2$ denoted as (9, 2), new stencil using $M = 7$ and $N = 3$ denoted as (7, 3) and rhombus stencil using $M = 4$ and $N = 4$ denoted as (4, 4) respectively. All the C-TSD-TEM, N-TSD-TEM, C-TSD-LSM and N-TSD-LSM are used in this discussion section. We compare accuracy by dispersion analysis and numerical modelling for a homogenous model.

First, we compare the accuracies by dispersion error analysis. The maximum error of $|\xi(\beta, \theta)|$ defined by eq. (20) along all propagation angles is used here to describe the dispersion. Fig. 22 displays the variations of $\zeta(\beta)$ with β for all the FD schemes mentioned above. For LS-based FD schemes, we use $\eta = 10^{-2.5}$ to search for the maximum wavenumber based on eq. (24). This maximum wavenumber is used to

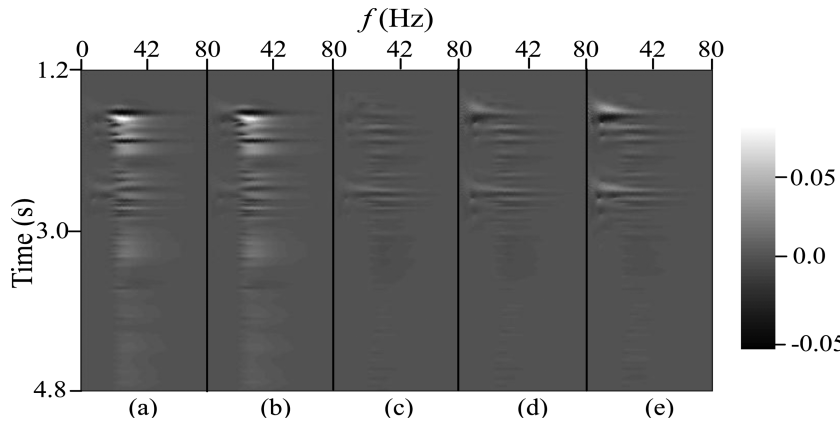


Figure 21. Globally normalized time–frequency envelope misfits between the reference waveform and numerical waveforms shown in Fig. 20. Panels (a)–(e) show the misfits between the red dashed waveforms shown in Figs 20(a)–(e) and reference waveform, respectively.

Table 2. List of the CPU time consumed by seven different kinds of schemes using the same maximum allowed dispersion error for the SEG/EAGE salt model.

Methods	CPU time
C-TSD-TEM with fixed spatial operator length scheme, $M = 33$, $\tau = 1$ ms	1025.682 s
N-TSD-TEM with fixed spatial operator length scheme, $M = 28$, $N = 3$, $\tau = 1$ ms	991.853 s
C-TSD-TEM with variable spatial operator length scheme, $M = 3\text{--}33$, $\tau = 1$ ms	625.134 s
N-TSD-TEM with variable spatial operator length scheme, $M = 3\text{--}28$, $N = 3$, $\tau = 2$ ms	331.017 s
C-TSD-LSM with variable spatial operator length scheme, $M = 2\text{--}14$, $\tau = 1$ ms	434.420 s
N-TSD-LSM with variable spatial operator length scheme, $M = 2\text{--}14$, $N = 2$, $\tau = 2$ ms	221.212 s
N-TSD-LSM with variable spatial operator length scheme, $M = 3\text{--}14$, $N = 3$, $\tau = 3$ ms	175.334 s

calculate the FD coefficients in eq. (25). When the given parameters are used, C-TSD-LSM (10, 1) is unstable. From Fig. 22, we can conclude that, N-TSD-LSM achieves smaller dispersion and wider wavenumber range than both the C-TSD-TEM and N-TSD-TEM. Of all the seven schemes, our N-TSD-LSM (7, 3) has the widest effective wavenumber range within which ζ is close to 0, thus it has the highest accuracy. For the TE-based schemes, dispersion of N-TSD-TEM (7, 3) is smaller than that of the other three methods and C-TSD-TEM (10, 1) exhibits the most significant dispersion error. Fig. 23 shows the snapshots at 1.2 s of those FD schemes. We observe significant dispersion in the snapshots of TE-based FD schemes shown in Fig. 23(a). By contrast, LS-based FD schemes can suppress the dispersion to some extent, especially our N-TSD-LSM (7, 3), which achieves nearly same accuracy as the reference solution. Those results are consistent with the conclusions we draw from the dispersion curves analysis.

By comparison, we conclude that, with the same grid points involved in the FD stencil, our N-TSD-LSM and N-TSD-TEM yield higher accuracy than C-TSD-TEM. Our new schemes suppress the spatial dispersion and temporal dispersion synchronously; thus it can effectively improve the modelling accuracy. Also, different combinations of parameters M and N provide different modelling accuracy. Theoretically

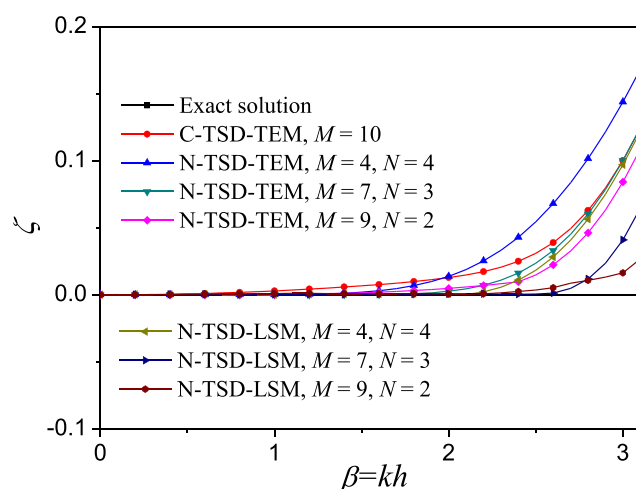


Figure 22. Variations of $\zeta(\beta) = \max_{\theta \in [0, \pi/4]} |\xi(\beta, \theta)|$ with β for C-TSD-TEM, N-TSD-TEM and N-TSD-LSM adopting the stencils that include the same number of grid points. $r = 0.45$. $\eta = 10^{-2.5} \approx 0.003$ is used in the N-TSD-LSM. The C-TSD-LSM is unstable for the given parameters.

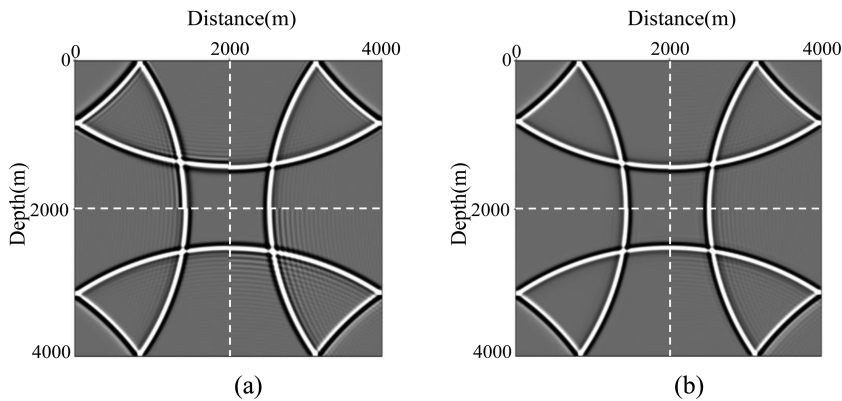


Figure 23. Snapshots at 1.2 s of a homogeneous model computed by FD schemes mentioned in Fig. 22. The model size is $4000 \text{ m} \times 4000 \text{ m}$. $\tau = 0.003 \text{ s}$, $h = 20 \text{ m}$, $v = 3000 \text{ m s}^{-1}$, $\eta = 0.001$ are used in the N-TSD-LSM. No ABCs are used. A Ricker-type wavelet with dominant frequency of 25 Hz is used in the centre of the model. (a) The C-TSD-TEM and N-TSD-TEM. (b) Reference and N-TSD-LSM. Each figure contains four equivalent panels corresponding to the snapshots of four different schemes. The left-upper, right-upper, left-bottom and right-bottom panels in panel (a) are computed by C-TSD-TEM with $M = 10$, N-TSD-TEM with $M = 9$ and $N = 2$, N-TSD-TEM with $M = 7$ and $N = 3$ and N-TSD-TEM with $M = 4$ and $N = 4$, respectively. (b) The right-upper, left-bottom and right-bottom panels are computed by N-TSD-LSM with $M = 9$ and $N = 2$, N-TSD-LSM with $M = 7$ and $N = 3$ and N-TSD-LSM with $M = 4$ and $N = 4$, respectively. The left-upper panel shows the reference solution.

speaking, the rhombus FD scheme can produce the greatest modelling accuracy when the same operator length is used. However, it is computationally expensive because $\sim M^2$ grid points, as opposed to $\sim M$ in conventional cross stencil, are involved. To suppress both the spatial dispersion and temporal dispersion and also to keep a balance between accuracy and efficiency, parameters M and N should be chosen carefully. Our experiments demonstrate that $N = 3$ is generally enough for the temporal accuracy and spatial accuracy can be increased by increasing parameter M . Further increasing N may help improve the modelling accuracy. However, the improvement is not significant. The high computational cost also convinces us that it is not worth doing this. Moreover, the N-TSD-LSM is more recommended than N-TSD-TEM because the latter is easier to suffer from dispersion.

Another issue is that, for models with large maximum velocity or large velocity contrasts, a very small time step, determined by the maximum velocity, has to be adopted to keep the modelling stable. With such constrained maximum allowed time steps, accuracy improvement of our new methods may diminish to some extent. Our experiment under such circumstance suggests that, N-TSD-TEM can have only slightly increased modelling accuracy compared to C-TSD-TEM, and they are all prone to the spatial dispersion. C-TSD-LSM can become unstable easily and much smaller time step than the maximum allowed value should be adopted. N-TSD-LSM can suppress both the temporal and spatial dispersions effectively, and can also use more flexible time step than C-TSD-LSM. Therefore, it can still show superiority. This superiority will gradually diminish with the increasing maximum velocity or velocity contrast for the fixed grid spacing and main source frequency.

7 CONCLUSIONS

We develop a novel FD stencil for modelling 2-D constant-density acoustic wave equation. The FD scheme based on this stencil is $(2M)$ th-order accurate in space and $(2N)$ th-order accurate in time when spatial FD coefficients and temporal FD coefficients are determined by their respective dispersion relation independently using TE. The accuracy is further increased by determining FD coefficients using the time–space-domain dispersion relation based on TE method or LS method. Dispersion analysis, stability analysis and modelling tests demonstrate that the new scheme has higher accuracy and better stability than the conventional scheme, and accuracy and stability can be further improved by increasing operator length parameter N in the new scheme, thus larger time steps can be used. Furthermore, LS-based FD coefficients yield higher accuracy than TE-based FD coefficients for our new FD scheme. Combining our new LS-based FD scheme using larger time steps and variable spatial operator length methods, the modelling efficiency is significantly improved. Our new schemes thus provide a powerful tool for large-scale and long-time seismic modelling and can be straightforwardly extended to the 3-D case.

ACKNOWLEDGEMENTS

This research is supported by the National Natural Science Foundation of China (NSFC) under contract number 41474110, the National High Technology Research and Development Program of China (863 Program) under contract number 2013AA064201. We thank editor Prof Jean Virieux, and two reviewers, Dr Peter Moczo and Dr Bing Zhou, for their valuable comments, which helped improve the quality of this paper. EW is also grateful for Shell's PhD scholarship to support excellence in geophysical research.

REFERENCES

- Bae, H.S., Pyun, S., Shin, C., Marfurt, K.J. & Chung, W., 2012. Laplace-domain waveform inversion versus refraction-traveltime tomography, *Geophys. J. Int.*, **190**, 595–606.
- Baysal, E., Kosloff, D.D. & Sherwood, J.W., 1983. Reverse time migration, *Geophysics*, **48**, 1514–1524.
- Carcione, J.M., Herman, G.C. & Ten Kroode, A.P.E., 2002. Seismic modeling, *Geophysics*, **67**, 1304–1325.
- Chen, J., 2007. High-order time discretizations in seismic modeling, *Geophysics*, **72**, SM115–SM122.
- Chen, J., 2009. Lax-Wendroff and Nyström methods for seismic modelling, *Geophys. Prospect.*, **57**, 931–941.
- Chu, C. & Stoffa, P.L., 2012. Implicit finite-difference simulations of seismic wave propagation, *Geophysics*, **77**, T57–T67.
- Dablain, M.A., 1986. The application of high-order differencing to the scalar wave equation, *Geophysics*, **51**, 54–66.
- Fang, G., Fomel, S., Du, Q. & Hu, J., 2014. Lowrank seismic-wave extrapolation on a staggered grid, *Geophysics*, **79**, T157–T168.
- Finkelstein, B. & Kastner, R., 2007. Finite difference time domain dispersion reduction schemes, *J. Comput. Phys.*, **221**, 422–438.
- Finkelstein, B. & Kastner, R., 2008. A comprehensive new methodology for formulating FDTD schemes with controlled order of accuracy and dispersion, *IEEE Trans. Antennas Propag.*, **56**, 3516–3525.
- Fornberg, B., 1987. The pseudospectral method: Comparisons with finite differences for the elastic wave equation, *Geophysics*, **52**, 483–501.
- Furumura, T. & Takenaka, H., 1996. 2.5-D modelling of elastic waves using the pseudospectral method, *Geophys. J. Int.*, **124**, 820–832.
- Geller, R.J. & Takeuchi, N., 1998. Optimally accurate second-order time-domain finite difference scheme for the elastic equation of motion: one dimensional case, *Geophys. J. Int.*, **135**, 48–62.
- Ghrist, M., Fornberg, B. & Driscoll, T.A., 2000. Staggered time integrators for wave equations, *SIAM J. Numer. Anal.*, **38**, 718–741.
- Ichimura, T., Hori, M. & Kuwamoto, H., 2007. Earthquake motion simulation with multiscale finite-element analysis on hybrid grid, *Bull. seism. Soc. Am.*, **97**, 1133–1143.
- Kosloff, D.D. & Baysal, E., 1982. Forward modeling by a Fourier method, *Geophysics*, **47**, 1402–1412.
- Kristekov'a, M., Kristek, J. & Moczo, P., 2009. Time-frequency misfit and goodness-of-fit criteria for quantitative comparison of time signals, *Geophys. J. Int.*, **178**, 813–825.
- Lax, P. & Wendroff, B., 1960. Systems of conservation laws, *Commun. Pure appl. Math.*, **13**, 217–237.
- Lele, S.K., 1992. Compact finite difference schemes with spectral-like resolution, *J. Comput. Phys.*, **103**, 16–42.
- Levander, A.R., 1988. Fourth-order finite-difference P-SV seismograms, *Geophysics*, **53**, 1425–1436.
- Liu, Y., 2013. Globally optimal finite-difference schemes based on least squares, *Geophysics*, **78**, T113–T132.
- Liu, Y., 2014. Optimal staggered-grid finite-difference schemes based on least-squares for wave equation modelling, *Geophys. J. Int.*, **197**, 1033–1047.
- Liu, Y. & Sen, M.K., 2009. A new time-space domain high-order finite-difference method for the acoustic wave equation, *J. Comput. Phys.*, **228**, 8779–8806.
- Liu, Y. & Sen, M.K., 2010. A hybrid scheme for absorbing edge reflections in numerical modeling of wave propagation, *Geophysics*, **75**, A1–A6.
- Liu, Y. & Sen, M.K., 2011. Finite-difference modeling with adaptive variable-length spatial operators, *Geophysics*, **76**, T79–T89.
- Liu, Y. & Sen, M.K., 2013. Time-space domain dispersion-relation-based finite-difference method with arbitrary even-order accuracy for the 2D acoustic wave equation, *J. Comput. Phys.*, **232**, 327–345.
- Liu, H., Dai, N., Niu, F. & Wu, W., 2014. An explicit time evolution method for acoustic wave propagation, *Geophysics*, **79**, T117–T124.
- Marfurt, K.J., 1984. Accuracy of finite-difference and finite-element modeling of the scalar and elastic wave equations, *Geophysics*, **49**, 533–549.
- McMechan, G.A., 1983. Migration by extrapolation of time-dependent boundary values, *Geophys. Prospect.*, **31**, 413–420.
- Mead, J.L. & Renaut, R.A., 1999. Optimal Runge–Kutta methods for first order pseudospectral operators, *J. Comput. Phys.*, **152**, 404–419.
- Moczo, P., Kristek, J. & Galis, M., 2014. *The Finite-Difference Modelling of Earthquake Motions: Waves and Ruptures*, Cambridge Univ. Press.
- Moczo, P., Kristek, J., Galis, M. & Pazak, P., 2010. On accuracy of the finite-difference and finite-element schemes with respect to *P*-wave to *S*-wave speed ratio, *Geophys. J. Int.*, **182**, 493–510.
- Moczo, P., Kristek, J., Galis, M., Chaljub, E. & Etienne, V., 2011. 3-D finite-difference, finite-element, discontinuous-Galerkin and spectral-element schemes analysed for their accuracy with respect to *P*-wave to *S*-wave speed ratio, *Geophys. J. Int.*, **187**, 1645–1667.
- Pratt, R.G., Shin, C. & Hicks, G.J., 1998. Gauss–Newton and full Newton methods in frequency-space seismic waveform inversion, *Geophys. J. Int.*, **133**, 341–362.
- Song, X. & Fomel, S., 2011. Fourier finite-difference wave propagation, *Geophysics*, **76**, T123–T129.
- Song, X., Fomel, S. & Ying, L., 2013. Lowrank finite-differences and lowrank Fourier finite-differences for seismic wave extrapolation in the acoustic approximation, *Geophys. J. Int.*, **193**, 960–969.
- Tam, C.K.W. & Webb, J.C., 1993. Dispersion-relation-preserving finite difference schemes for computational acoustics, *J. Comput. Phys.*, **107**, 262–281.
- Tan, S. & Huang, L., 2014a. A staggered-grid finite-difference scheme optimized in the time–space domain for modeling scalar-wave propagation in geophysical problems, *J. Comput. Phys.*, **276**, 613–634.
- Tan, S. & Huang, L., 2014b. An efficient finite-difference method with high-order accuracy in both time and space domains for modelling scalar-wave propagation, *Geophys. J. Int.*, **197**, 1250–1267.
- Tarantola, A., 1984. Inversion of seismic reflection data in the acoustic approximation, *Geophysics*, **49**, 1259–1266.
- Virieux, J., 1984. SH-wave propagation in heterogeneous media: velocity–stress finite-difference method, *Geophysics*, **49**, 1933–1942.
- Virieux, J. & Operto, S., 2009. An overview of full-waveform inversion in exploration geophysics, *Geophysics*, **74**, WCC1–WCC26.
- Virieux, J., Calandra, H. & Plessix, R.É., 2011. A review of the spectral, pseudo-spectral, finite-difference and finite-element modelling techniques for geophysical imaging, *Geophys. Prospect.*, **59**, 794–813.
- Wang, Y., Liang, W., Nashed, Z., Li, X., Liang, G. & Yang, C., 2014. Seismic modeling by optimizing regularized staggered-grid finite-difference operators using a time–space-domain dispersion-relationship-preserving method, *Geophysics*, **79**, T277–T285.
- Yang, D., Chen, S. & Li, J., 2007. A Runge–Kutta method using high-order interpolation approximation for solving 2D acoustic and elastic wave equations, *J. Seism. Explor.*, **16**, 331–353.
- Zhang, J. & Yao, Z., 2012a. Globally optimized finite-difference extrapolator for strongly VTI media, *Geophysics*, **77**, T125–T135.
- Zhang, J. & Yao, Z., 2012b. Optimized finite-difference operator for broadband seismic wave modeling, *Geophysics*, **78**, A13–A18.
- Zhang, Z., Zhang, W. & Chen, X., 2014. Stable discontinuous grid implementation for collocated-grid finite-difference seismic wave modelling, *Geophys. J. Int.*, **199**, 860–879.
- Zhou, H. & Zhang, G., 2011. Prefactored optimized compact finite-difference schemes for second spatial derivatives, *Geophysics*, **76**, WB87–WB95.

APPENDIX

This appendix demonstrates that our new FD scheme determining the coefficients using eq. (15) can achieve $(2N)$ th-order modelling accuracy along all directions.

The total error of eq. (9) is

$$\varepsilon = \frac{1}{h^2} \left| a_{0,0} + 2 \sum_{m=1}^M a_{m,0} [\cos(mk_x h) + \cos(mk_z h)] + 4 \sum_{m=1}^{N-1} \sum_{n=1}^{N-m} a_{m,n} [\cos(mk_x h) \cos(nk_z h)] - \frac{h^2}{v^2 \tau^2} [-2 + 2 \cos(w\tau)] \right|. \quad (\text{A1})$$

Using eqs (12)–(14), eq. (A1) is transformed as

$$\begin{aligned} \varepsilon &= \frac{2}{h^2} \left| \sum_{j=M+1}^{\infty} (-1)^j \left[\sum_{m=1}^M a_{m,0} \frac{m^{2j}(k_x^{2j} + k_z^{2j})}{(2j)!} + 2 \sum_{m=1}^{N-1} \sum_{n=1}^{N-m} a_{m,n} \frac{(m^{2j}k_x^{2j} + n^{2j}k_z^{2j})}{(2j)!} \right] h^{2j} \right. \\ &\quad \left. + 2 \sum_{\xi=1}^{N-1} \sum_{\xi=N+1-\xi}^{\infty} \left[\sum_{m=1}^{N-1} \sum_{n=1}^{N-m} a_{m,n} \frac{(-1)^{\xi+\xi} m^{2\xi} n^{2\xi} k_x^{2\xi} k_z^{2\xi}}{(2\xi)!(2\xi)!} \right] h^{2\xi+2\xi} \right. \\ &\quad \left. + 2 \sum_{\xi=N}^{\infty} \sum_{\xi=1}^{\infty} \left[\sum_{m=1}^{N-1} \sum_{n=1}^{N-m} a_{m,n} \frac{(-1)^{\xi+\xi} m^{2\xi} n^{2\xi} k_x^{2\xi} k_z^{2\xi}}{(2\xi)!(2\xi)!} \right] h^{2\xi+2\xi} \right. \\ &\quad \left. - \sum_{j=M+1}^{\infty} \left[\frac{(-1)^j r^{2j-2}(k_x^{2j} + k_z^{2j})}{(2j)!} \right] h^{2j} - \sum_{j=N+1}^{\infty} \sum_{\xi=1}^{j-1} \left[\frac{(-1)^j r^{2j-2} k_x^{2j-2\xi} k_z^{2\xi} (j)!}{(2j)!(\xi)!(j-\xi)!} \right] h^{2j} \right| \\ &\approx \frac{2}{h^2} [o(h^{2M+2}) + o(h^{2N+2}) + o(h^{2N+2}) + o(h^{2M+2}) + o(h^{2N+2})] \approx o(h^{2N}). \end{aligned} \quad (\text{A2})$$

In eq. (A2), the minimum power of h is $2N$, therefore, the modelling accuracy is $(2N)$ th-order.